



Valence-Tuned Lithium Titanate Nanopowder for High-Rate Electrochemical Energy Storage

Mathias Widmaier,^[a, b] Kristina Pfeifer,^[a, c] Lars Bommer,^[a] and Volker Presser^{*[b, d]}

In recent years, numerous studies have explored ways to overcome the low intrinsic electrical conductivity of lithium titanate ($\text{Li}_4\text{Ti}_5\text{O}_{12}$, LTO) for energy storage with lithium-ion batteries. These approaches almost exclusively considered element doping and elaborate LTO-carbon nanocomposites, whereas simple adjustment of the defect concentration remains largely unexplored. In our study, we tune the $\text{Ti}^{3+}/\text{Ti}^{4+}$ concentration of a commercial LTO nanopowder through oxygen vacancy formation during thermal annealing in hydrogen atmosphere. We investigate the impact of the treatment on material properties like energy band structure, electrical conductivity, crystallinity, phase distribution, surface chemistry, and particle morphology, and correlate these parameters to the

electrochemical performance. At optimum treatment conditions, the intrinsic electrical conductivity can be greatly improved, while circumventing LTO phase transformations or amorphization. This enables the reduction of the carbon concentration to 5 mass%, while yielding a high electrode capacity of about 70 mAh/g (82 mAh/g based on active mass) at ultrahigh C-rates of 100C. When combined with an activated carbon/lithium manganese oxide composite cathode, an excellent energy and power performance of 70 Wh/kg and 47 kW/kg were obtained (82 Wh/kg and 55 kW/kg based on active mass), while maintaining 83% of its energy ratings after 5000 cycles at 10C (78% after 15000 cycles at 100C).

1. Introduction

Lithium-ion batteries and supercapacitors have become indispensable energy storage devices for the steadily growing electrification.^[1] Lithium-ion batteries store energy via reversible Faradaic reactions and related lithium intercalation/de-intercalation into host materials.^[2] On the contrary, the operating principle of a conventional supercapacitor is based on ion electrosorption at the interface of an electrolyte and high surface area electrodes, such as activated carbon (AC).^[3] These energy storage principles are reflected by the inherently different properties of both devices: A lithium-ion battery is a high energy device with moderate power and longevity, while a supercapacitor possesses a superior power density and cycle life with an inferior energy density.^[4] To overcome the intrinsic limitations of each of these two technologies, device hybridization has been explored in recent years.^[5–14]

Hybrid supercapacitors, combining the advantages of both devices, were first introduced in a pioneering study of Amatucci et al.^[5] In this work, an asymmetric hybrid supercapacitor

combined an AC cathode with a lithium titanate anode. Hybridization can also be realized by combining lithium-ion battery materials with AC in the same electrode. These composite electrodes have attracted considerable interest in the scientific community and several material combinations have been proposed.^[6–14] Additionally beneficial synergistic effects between both material classes have been observed, as AC simultaneously decreases the electrode resistivity and can act as a “shock absorber” for high currents.^[7,12]

LTO is a promising lithium-ion battery electrode material for high rate applications due to its inherent safety, high Coulombic efficiency, negligible volume expansion during lithiation, cost effective raw materials for synthesis, and effective avoidance of the solid electrolyte interphase (SEI) formation.^[15–17] The electrochemical behavior of LTO-based electrodes may severely deteriorate because of LTO’s poor intrinsic electronic conductivity of about 10^{-13} S/cm.^[14,18] However, there is an abrupt rise of electrical conductivity for lithiated LTO ($\text{Li}_x\text{Ti}_5\text{O}_{12}$) to about 10^{-2} S/cm.^[19] At present, state-of-the-art literature appears to have split into two camps:

- i.) The electrical conductivity of the lithiated phase ($\text{Li}_x\text{Ti}_5\text{O}_{12}$) is sufficiently high to operate LTO without any or very low amounts of conductive additives (< 5 mass%).^[20–25] Kinetic limitations of LTO are mainly caused by sluggish lithium diffusion and an improvement of electrical conductivity is not required.^[25,26]
- ii.) The low electrical conductivity of $\text{Li}_x\text{Ti}_5\text{O}_{12}$ deteriorates the electrochemical performance and large amounts of carbon are required for high rate operation. In this context, a variety of LTO-carbon nanocomposites have been proposed; for example, LTO confined in nanopores of AC,^[27] and LTO grafted on carbon nanotubes,^[28–32] carbon nanofibers,^[17,33–35] or graphene.^[36–40] The carbon content of the electrode is

[a] M. Widmaier, K. Pfeifer, Dr. L. Bommer
Robert Bosch GmbH, Robert-Bosch-Campus 1, 71272 Renningen, Germany

[b] M. Widmaier, Prof. V. Presser
Department of Materials Science and Engineering, Saarland University,
Campus D2 2, 66123 Saarbrücken, Germany
E-mail: volker.presser@leibniz-inm.de

[c] K. Pfeifer
Chemisches Institut, Eberhard Karls Universität Tübingen, Auf der Morgenstelle 18, 72076 Tübingen, Germany

[d] Prof. V. Presser
INM – Leibniz Institute for New Materials, Campus D2 2, 66123 Saarbrücken, Germany

 Supporting Information and the ORCID identification number(s) for the author(s) of this article can be found under:
<https://doi.org/10.1002/batt.201700007>

often neglected when calculating the capacity (i.e., capacity is only normalized to the LTO mass of the electrode). Yet, such a normalization is questionable as the electrode may contain up to 20–50 mass% carbon and only the performance of the entire electrode is of importance for an actual device (not how well a small quantity of LTO performs in a massive matrix of electrochemically inactive carbon).

The electrical conductivity of carbon and its distribution can also severely influence the electrochemical stability of a composite electrode as we have demonstrated recently.^[14] LTO doping (e.g., with Cu²⁺,^[41] Mg²⁺,^[42] Zn²⁺,^[43] Fe³⁺,^[44] Cr³⁺,^[45] Al³⁺,^[46] Sn⁴⁺,^[47] Zr⁴⁺,^[48] Ta⁵⁺,^[49] V⁵⁺,^[50] Nb⁵⁺,^[51] W⁶⁺,^[52]) is another effective way to improve the intrinsic electronic conductivity of LTO. Such doping elements have been reported to reduce a fraction of Ti⁴⁺ into Ti³⁺ and hence increase the overall electron concentration.^[53] Nevertheless, element doping might entail additional problems related to the toxicity of certain doping elements and possible detrimental side reactions.^[54]

In 2006, Wolfenstine et al.^[55] discovered that Ti³⁺ valence states may form during prolonged annealing (36 h) of LTO at 800 °C in hydrogen containing atmosphere, although the root cause of this effect remained unknown. This simple strategy is free of waste products and does not require the addition of any other additional chemicals or catalysts,^[56] but has only attracted little attention in literature so far (especially in contrast to the large number of studies addressing carbon-LTO nanocomposites or LTO doping). Shen et al.^[57] proposed annealing of LTO nanowire arrays under hydrogen atmosphere to create Ti³⁺ valence states. A minor shift of the Ti 2p X-ray photoelectron spectra to lower binding energies after hydrogen treatment confirmed the formation of Ti³⁺ valences. This change was attributed to the formation of OH surface defects after hydrogen treatment. Hydrogen treatment was conducted in 5 vol% H₂ in Ar at 500–700 °C for 1.5 h, while the pressure or the impact of the treatment temperature was not specified. Later work of Qiu et al.^[56] was conducted with industrial grade LTO in high purity H₂ gas sourced from a metal-hydride at a high pressure of 40 bar for 1 h. It was suggested that the elevated temperature "facilitates the opening of the LTO lattice" while the high pressure "helps the deep penetration of hydrogen into the LTO bulk".^[56] In this work, it was also proposed that, besides OH groups, additionally oxygen vacancies are responsible for the Ti³⁺ valence states and the improvement of the rate performance. The enhanced electrochemical kinetics were attributed to increased electronic conductivity caused by Ti³⁺ valence states and a simultaneously improved Li-ion diffusivity due to larger diffusion pathways in the oxygen-deficient LTO. Sen et al. conducted hydrogen annealing of LTO nanosheets at 500 °C for 2 h with a heating rate 3 °C min⁻¹ (pressure not stated) and concluded that "the introduction of Ti³⁺ species and/or oxygen vacancies greatly improves the electronic conductivity".^[58] Accordingly, current literature on this topic seems to be inconsistent even on basic aspects like necessity of pressure, temperature range of the reaction, and the underpinning processes causing Ti³⁺ valence states.

In the current study, we address these issues and provide comprehensive data to identify crucial temperature ranges of the reaction. The associated implications on material and chemical properties (e.g., crystallinity, surface area, particle size, phase contents, titanium valence state) will be investigated and connected to the electrochemical behavior of LTO half cells and LTO-based hybrid supercapacitors. For this purpose, a commercially available lithium titanate nanopowder was heated to defined temperatures in hydrogen atmosphere, followed by an immediate cooling to preserve prevailing material properties. This allows us to adjust the concentration of Ti³⁺ valences and to identify the rate limiting factor of a nanoparticulate LTO electrode.

Experimental Section

Electrode Materials and Electrode Preparation

Steam-activated, coconut-derived activated carbon (AC) powders YP-50F and YP-80F were purchased from Kuraray Chemicals. Carbon black (CB) type C-NERGY C65, referred to as CB, was obtained from Imerys Graphite & Carbon. Commercial lithium manganese oxide (LMO, type: HPM-7051) and nanometer-sized lithium titanate (LTO, type: lithium titanate, spinel, nanopowder) was obtained from Toda Kogyo and Sigma Aldrich, respectively.

LTO was modified in a high temperature furnace (FSW 230/400-1500-MO/BL/PS, FCT Anlagenbau GmbH) by heating under hydrogen at atmospheric pressure with 10 °C min⁻¹ from room temperature to 500 °C, 600 °C, 800 °C, 900 °C, or 1000 °C and a hydrogen flow rate of 2 L min⁻¹. The samples were labelled L (pristine powder), L/500, L/800, L/900, and L/1000, respectively. Afterwards, the gas flow was switched to Ar with a flow rate of 2 L/min and the samples were cooled to room temperature at a rate of 20 °C/min without any temperature holding steps to preserve the prevailing material properties. After heat-treatment, the samples were immediately transferred into an Ar-filled glovebox (MBraun, O₂ and H₂O < 1 ppm) until further use to avoid a re-oxidation of the material.

For negative electrodes, LTO powder was mixed with different ratios of CB (Table 1) and 10 mass% polyvinylidene fluoride (PVdF) dissolved in dimethyl sulfoxide in a DAC400 FVZ speed-mixer. Subsequently, the electrode slurries were doctor bladed on a carbon-coated aluminum foil current collector (Ranafoil from Toyo Aluminium). The electrode sheets were dried for two days at ambient conditions in a fume hood, followed by drying in vacuum at 120 °C for 12 h. Finally, the dried electrodes were transferred and stored in an Ar-filled glovebox (MBraun, O₂ and H₂O < 1 ppm). Dried negative electrodes typically possessed a thickness of 25 ±

Table 1. Overview of the employed anode recipes and labeling.

Sample	LTO material	LTO content [mass%]	CB content [mass%]	PVdF content [mass%]
0-L	Pristine	90	0	10
5-L	Pristine	85	5	10
20-L	Pristine	70	20	10
5-L/500	500 °C in H ₂	85	5	10
5-L/600	600 °C in H ₂	85	5	10
5-L/800	800 °C in H ₂	85	5	10
5-L/900	900 °C in H ₂	85	5	10
5-L/1000	1000 °C in H ₂	85	5	10

5 µm with a material loading of 3 ± 1 mg/cm². The different negative electrode compositions are distinguished by a number, which reflects the CB content in mass percent, followed by the addition “-L” (pristine powder) or “-L/X” where “X” is the treatment temperature in °C of the respective modified LTO powder (Table 1).

Positive electrodes were produced by mixing 4.4 g activated carbon (YP-80F) with 2.4 g lithium manganese oxide, 0.4 g CB, and 0.8 g PVDF in dimethyl sulfoxide utilizing the same electrode preparation process as for negative electrodes. The dry electrode thickness was adjusted to 128 ± 10 µm at a material loading of 7 ± 1 mg/cm².

The counter electrode was prepared by mixing YP-50F with isopropanol in a DAC400 FVZ speed mixer at 2500 rpm.^[59] This treatment was followed by 7 min sonication and subsequent 4 min mixing at 2500 rpm. Afterwards, the slurry was transformed to a paste by adding 10 mass% (dry mass) of dissolved polytetrafluoroethylene (PTFE, 60 mass% solution in water from Sigma Aldrich) combined with speed-mixing at 800 rpm for 5 min. This paste was manually kneaded on a glass plate until the consistency of the paste was sufficiently viscous for further processing. An appropriate amount of electrode paste was placed between two untreated aluminum foils. This stack was then calendered in a BLE682 battery lamination machine by applying a mass of 70 kg and a forward speed of 10 mm/s.

We used a dry electrode preparation process inside an argon-filled glovebox (MBraun, O₂ and H₂O < 1 ppm) to manufacture quasi-reference electrodes (QRE) based on surface-functionalized AC, as outlined in more detail in Ref. [59]. Functionalization of AC was conducted in a nitric acid solution at 95 °C for 5 h according to our procedure described in Ref. [59]. The functionalization of AC introduces nitrogen and oxygen containing functional groups on the carbon surface, which drastically stabilize the QRE stability.^[59] The functionalized AC and PTFE powders (PTFE 6 CN X, DuPont) were dried at 120 °C under vacuum for 12 h before being introduced to the glovebox. Afterwards, 0.45 g carbon powder was mixed with 0.05 g PTFE and grinded in a mortar until a dry paste had formed. Small parts of the latter were then cut and used as QRE. For convenience and comparability to literature, all QRE potentials stated in this work were calculated to the Li potential.^[59]

Cell Preparation and Electrochemical Measurements

For electrochemical testing, we employed a custom-built polyether ether ketone (PEEK) cell with spring-loaded titanium pistons as a three-electrode system, as described in Ref. [60]. Electrode discs with 12 mm diameter were punched out of the electrode films and separated by a glass-fiber (Whatman GF/D) or cellulose separator (Nippon Kodoshi) for half-cell cycle life, or half-cell rate capability measurements and full-cells, respectively. The mass ratio of anode/cathode of full-cells was adjusted to 0.37. For half-cell cycle life measurements, two counter electrodes (525 ± 20 µm each) were pressed together and placed on a carbon-coated aluminum foil current collector (Ranafoil, Toyo Aluminium). In case of half-cell rate capability measurements, one counter electrode was used instead. The assembled cells were dried at 120 °C for 12 h at 0.1 Pa and then transferred to an Ar-filled glovebox (MBraun, O₂ and H₂O < 1 ppm). After cooling, the QRE was placed on a compressed glass-fiber separator (GF/D, from Whatman) in a cavity close to the working electrode/counter electrode stack and contacted by a titanium wire. Afterwards the cells were vacuum-filled with 1 M LiClO₄ dissolved in acetonitrile (99.9%, water content < 10 ppm, Acros Organics). In addition, individual electrodes were arranged between titanium positions without the addition of electrolyte, and

a current of 0.001 mA was applied to probe the electrical percolation.

Electrochemical measurements were carried out using a potentiostat/galvanostat CTS LAB from BaSyTec. Cyclic voltammetry was recorded with a sweep rate of 0.1 mV/s from 1.17–2.37 V. Galvanostatic charge/discharge cycling with potential limitation (GCPL) experiments were conducted at 1.17–2.37 V vs. Li/Li⁺ for half-cells and at 0.8–2.8 V for full-cells. The C-rate was calculated from the theoretical capacity of LTO (175 mAh/g, Ref.[16]). Half-cell rate capability measurements were conducted at C-rates between 0.1C and 200C (same rates for charge and discharge). Full-cells were cycled at 10C for 100 charge-discharge cycles and then charged at 1C prior to discharging at C-rates between 1C and 1000C. All electrochemical stability measurements were conducted at 10C charge/discharge rates. The first 100 cycles were recorded in sequence, followed by recording every 100th cycle until reaching 5000 cycles. All capacity, energy density, and power density values stated in this work are given with respect to the entire electrode mass if not otherwise mentioned and all electrochemical measurements were conducted at 23 ± 1 °C.

Material Characterization

Thermogravimetric measurements combined with a mass spectrometer (TGA-MS) were performed using a STA 409CD – QMS422 from Netzsch under Ar. For measurements using 60% H₂ and 40% He, a STA 429CD from Netzsch coupled with an analytical mass spectrometer QMG 422 from Balzers was used instead. The samples were heated to 1000 °C at a rate of 10 °C/min in the respective atmospheres.

Scanning electron microscopy (SEM) analysis was carried out with a SUPRA VP system from Zeiss at an acceleration voltage of 5 kV. The samples were mounted on a carbon tab and sputter coated with a thin layer of platinum/palladium prior to the investigation.

Transmission electron microscopy (TEM) was performed with a JEOL 2100F system operating at 120 kV. Samples were prepared by dispersing and sonicating of the powder samples in isopropanol and deposition on a copper grid with a lacey carbon film (Gatan).

Nitrogen gas sorption measurements of the carbon powders were carried out with an Autosorb iQ system (Quantachrome), at the temperature of liquid nitrogen (−196 °C) after outgassing (at 300 °C for 24 h) at about 10² Pa. The relative pressure range was varied from $5 \cdot 10^{-7}$ to 1.0 in 68 steps. The specific surface area (SSA) was calculated with the ASiQwin-software using the Brunauer-Emmett-Teller (BET) equation^[61] in the linear pressure range from 0.01–0.2. Values for the total pore volume correspond to $p/p_0 = 0.95$.^[62]

UV-Vis-NIR diffuse reflectance measurements were recorded at 250–2500 nm employing a Cary 5000 UV-Vis-NIR spectrometer (Agilent) with an integrating sphere (Labsphere). Powder samples with a thickness of about 500 µm were sandwiched between quartz glass. The reflectance of the quartz glass was subtracted from all measured spectra.

X-ray diffraction (XRD) experiments were conducted using a D8Advance DaVinci-Cu diffractometer (Bruker AXS) with a CuK α X-ray source, a Bragg-Brentano geometry, a 0.5° aperture stop, and a LynxEye detector. Rietveld refinement was carried out using TOPAS software (Bruker AXS).

X-ray photoelectron spectroscopy (XPS) was carried out with a PHI Quantera SXM utilizing monochromatic AlK α emission with an energy of 1486.6 eV for excitation (50 W, 200 µm spot diameter) and an angle between sample and analyzer of 45°. Survey spectra were recorded with a step size of 0.8 eV and a pass energy of

224 eV. For high resolution C 1 s and O 1 s spectra, a step size of 0.05 eV and a pass energy of 55 eV were used instead. The C 1 s maximum which was shifted to 285 eV to calibrate the binding energies of all recorded spectra. Before the measurements, the powder samples were pressed with a steel roller onto indium foils. Immediately afterwards, the samples were introduced into an ultrahigh vacuum.

2. Results and Discussion

2.1. Thermal Annealing of LTO in Hydrogen Atmosphere

A reduction of the LTO titanium oxidation state in hydrogen atmosphere can be explained by the reaction of hydrogen with lattice oxygen to form oxygen vacancies and water (Eq. 1) or by the creation of proton defects (Eq. 2). These two reactions can be expressed by use of the Kröger-Vink notation as follows:



Both reactions will lead to mass changes of LTO during annealing under hydrogen: Eq. 1 causes a mass decrease and Eq. 2 a slight mass increase. We measured TG-MS in hydrogen and argon atmosphere (Figure 1) to gain more insights into mechanisms and relevant temperature ranges of the reaction. Below 450 °C, we observed three distinct regions of mass loss when thermally annealing in argon and in hydrogen atmosphere. These mass changes must be connected to intrinsic reactions of LTO during thermal annealing, rather than arising from specific reactions of LTO with hydrogen. In the first and second region, water desorbs from the sample (Figure 1B) with maximum rates of mass change centered at 86 °C and 223 °C, respectively. The low temperature desorption is correlated to the release of physisorbed water from the surface, while water desorption at 223 °C is likely connected to the recombination of OH groups. This temperature aligns with values reported for

recombination in TiO₂ for OH by Henderson (217 °C; Ref. [63]) and Hugenschmidt et al. (227 °C; Ref. [64]). At about 400 °C, a third reaction takes place which releases CO₂. Additionally, small amounts of CO₂ desorb in the temperature range of 150–350 °C. The CO₂ desorption could be related to decomposition of carboxylic groups at the LTO surface and/or of impurities.

At temperatures exceeding 450 °C, the behavior of LTO annealed in either argon or hydrogen starts to deviate. In argon atmosphere, no further decomposition reaction is detected, as the mass remains constant (Figure 1A) and no gaseous species were observed. By contrast, after annealing in hydrogen, we see a continued mass loss and a simultaneous water desorption at 450–1000 °C. Hence, we can correlate this temperature range to the reaction according to Eq. 1. A shoulder of the differential thermogravimetry (DTG) curve at 813 °C and an additional small peak at 940 °C indicate a possible transition of the type of reaction mechanism in the range of 800–900 °C. Oxygen may initially be removed from low energy lattice sites until reaching the maximum reaction rate at about 813 °C. With increasing the reaction temperature, these oxygen positions continuously deplete and are replaced by oxygen vacancies. Thereby, the reaction rate is being reduced and a shoulder of the DTG curve is observed. For temperatures above 800 °C, the thermal energy is sufficient to also activate the removal of oxygen located at high-energy positions and the reaction rate re-accelerates until reaching its maximum at 940 °C.

Based on these observations, we annealed LTO at 500 °C (reaction start), 600 °C (early stage of reaction), 800 °C (DTG shoulder), 900 °C (transition area to second high-temperature DTG peak), and 1000 °C (post second high-temperature DTG peak) in a furnace under hydrogen atmosphere to produce appropriate quantities of modified LTO for further experiments. For all annealing experiments, we chose conditions alike applied during the TG measurements for a meaningful comparability (i.e., same heating rate, no temperature holding steps, gas flow switched to Ar during cooling to preserve the prevailing material properties). The samples treated in the furnace show a mass loss as would be expected from the TG measurement (Figure 1A). A slightly higher mass than what we

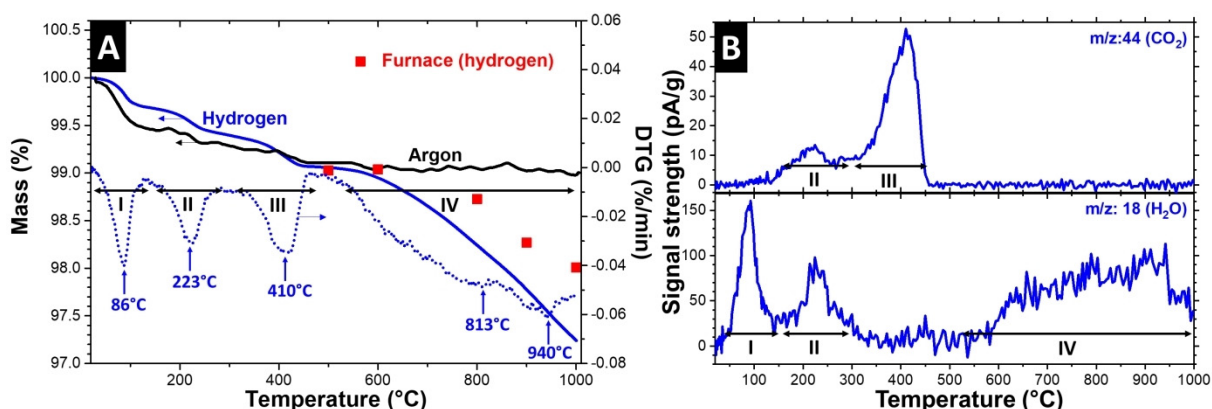


Figure 1. (A) Thermogravimetric and derivative thermogravimetric (DTG) curve of LTO powder during thermal annealing under argon and hydrogen atmosphere. The red markers correspond to mass loss measured after treatment of LTO in a high temperature furnace under hydrogen atmosphere. (B) Mass spectra signals of the gasses evolving during annealing under hydrogen atmosphere.

measured with the thermogram for high-temperature treated samples (L/800, L/900, and L/1000) could be indicative to absorption of gaseous species and a minor re-oxidation during follow-up sample transfer (in air).

Our results confirm a mechanism according to Eq. 1. Nevertheless, proton defects cannot be entirely excluded according to the TG-MS results, as hydrogen absorption according to Eq. 2 could be masked by the observed oxygen removal, especially when considering the large mass difference between hydrogen and oxygen. The presence of large amounts of OH groups is relatively unlikely due to the tendency of OH groups to condensate into water and oxygen vacancies during thermal annealing.^[63] Shin et al.^[54] concluded that oxygen vacancies account for the majority of crystal structure defects for hydrogen treated TiO_2 , as proton defects would equilibrate quickly due to the much higher mobility as compared to oxygen vacancies.^[54] Hence, proton defects likely play a minor role for hydrogen treated LTO. The strong hydrogen signal reported by Qiu et al.^[56] using nuclear magnetic resonance (NMR) spectroscopy could be caused by chemisorbed water due to the high tendency for water absorption of the oxygen-deficient samples caused by the reasons described above, rather than originating from OH-groups formed during hydrogen treatment. Moreover, oxygen-deficient LTO (Ref. [65]) and TiO_2 (Ref. [66]) surfaces have been reported to immediately form OH groups after exposure to atmospheric water due to the high hydrophilicity of Ti^{3+} .^[67] This trend is also supported by our XPS characterization below.

We have calculated the chemical composition and oxidation state of Ti according to the mass loss of the thermogram recorded at 450–1000 °C for LTO annealed in hydrogen (Table 2) by assuming Eq. 1 and LTO phase preservation. A mass loss of 1% at a moderate temperature of 800 °C appears relatively small. Yet, this value translates to about 0.25 oxygen ions removed per LTO structural unit, as phase preservation can be assumed at this temperature (see XRD characterization). Thereby, every eighth titanium ion was reduced from Ti^{4+} to Ti^{3+} at 800 °C. Accordingly, significant modifications of electronic properties of the electrode material are anticipated. Furthermore, enough Ti^{4+} remains for the electrochemical reaction: three out of five Ti^{4+} ions have to be reduced to Ti^{3+} during lithiation to attain the full theoretical capacity of 175 mAh/g.^[16]

Table 2. Temperature dependent mass change of LTO at different temperatures with respect to a temperature of 450 °C and calculated oxygen loss, theoretical LTO formula unit with average Ti oxidation state (OS), number (#) of Ti^{3+} respectively Ti^{4+} ions per LTO formula unit, and $\text{Ti}^{3+}/\text{Ti}^{4+}$ ratio assuming LTO phase preservation.

Temperature [°C]	Mass [%]	O loss [%]	Formula unit	Avg. Ti	# Ti^{4+}	# Ti^{3+}	# $\text{Ti}^{3+}/\text{Ti}^{4+}$ OS
500	99.99	0.02	$\text{Li}_4\text{Ti}_5\text{O}_{12}$	4.00	4.99	0.01	<0.01
600	99.88	0.29	$\text{Li}_4\text{Ti}_5\text{O}_{11.97}$	3.99	4.93	0.07	0.01
800	99.17	1.98	$\text{Li}_4\text{Ti}_5\text{O}_{11.76}$	3.90	4.52	0.48	0.11
900	98.71	3.08	$\text{Li}_4\text{Ti}_5\text{O}_{11.63}$	3.85	4.26	0.74	0.17
1000	98.17	4.38	$\text{Li}_4\text{Ti}_5\text{O}_{11.47}$	3.79	3.95	1.05	0.27

2.2. Material Characterization of Reduced LTO Powders

The LTO investigated in this study predominantly consists of branched chains of fused LTO nanoparticles with about 50 nm diameter, as can be seen from electron micrographs depicted in Figure 2A. This microstructure benefits rapid electrolyte penetration through the open pore network and simultaneously increases the overall electrolyte-electrode interface area. Accordingly, the Li-diffusion distance in the solid state is decreased and fast charge and discharge rates are enabled. A small number of larger particles with a diameter $\leq 1 \mu\text{m}$ in the network of LTO nanoparticles can be seen from the scanning electron micrographs. The particle morphology is largely maintained for modification temperatures of up to 800 °C, as no changes were observed by SEM and TEM characterization (Figure 2A–D). However, a stark impact on the optical material properties can be seen, as the powder changed its color from white to light blue and then to blue. At temperatures above 800 °C, distinct changes of the powder microstructure occur, since the powder density starts to rise markedly (Figure 2E–F). Simultaneously, the color of the samples transforms into dark blue (900 °C) and finally to black (1000 °C). The LTO nanoparticles start to coalesce to larger primary particles with a diameter of about 100 nm at 900 °C (Figure 2E, inset). When adjusting the temperature to 1000 °C, all LTO nanoparticles were transformed into micrometer-large particles with some internal porosity (Figure 2F).

Figure 3A shows the optical absorption spectra of the different LTO samples. The pristine powder exhibits absorption below 420 nm (3 eV), with its main absorption edge in the ultraviolet region at about 320 nm (3.9 eV). Accordingly, the pristine powder appears white, as light in the visible range is almost entirely reflected. This absorption energy range is typical for wide-band-gap semiconductors and corresponds to electron excitation from the filled valence band into the empty conduction band.^[68] The theoretical band gap of LTO was calculated to be 2.0–2.3 eV,^[69,70] but experimentally obtained results in the range of 3–7 eV align with our findings.^[68,71–73] After heat treatment at 500 °C in hydrogen atmosphere, a wide absorption band arises centered at around 1200 nm (1 eV). When further increasing the treatment temperature to 600 °C, this absorption band becomes more pronounced and broader. For temperatures exceeding 800 °C, the expansion leads to near 100% absorption in the low energy range up to 2500 nm (0.5 eV) and a small area at 320–800 nm with only minor absorption. This behavior strongly suggests additional absorption in the wavelength region beyond our experimental limitation of 2500 nm. For highly modified powders (i.e., L/900 and L/1000), absorption at 320–800 nm is further increased and near 100% absorption over all investigated wavelengths can be observed for L/1000. We attribute the absorption band to electron transitions from intra-band-gap energy levels (in-gap states) to the conduction band.^[74] Such in-gap-states have been reported for oxygen-deficient LTO (Ref. [56]) and TiO_2 (Ref. [74–76]) and are related to oxygen vacancy formation and associated Ti^{3+} valence states. Our results suggest that the in-gap states initially occur at about 1 eV below the conduction

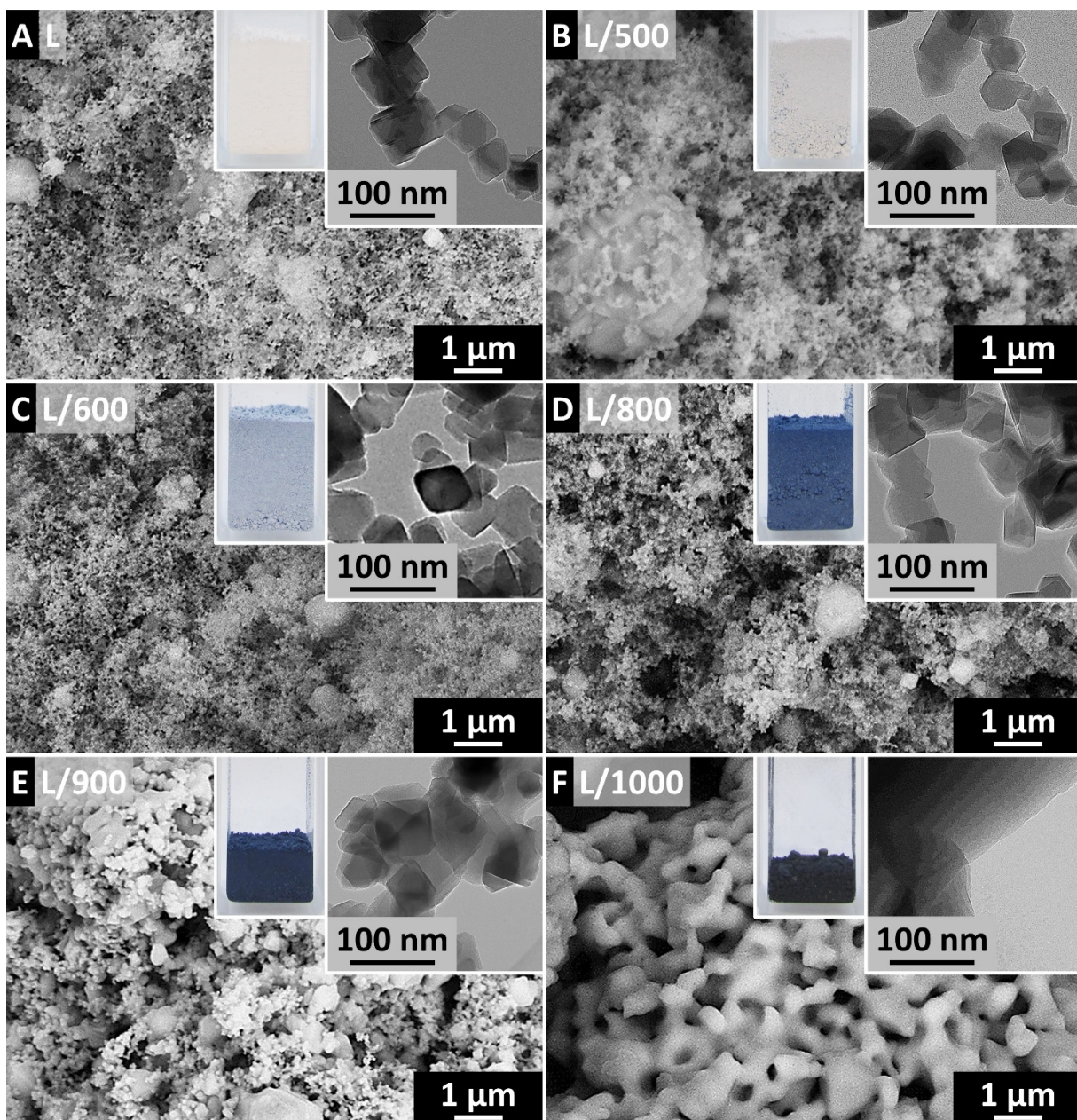


Figure 2. SEM and TEM (inset) micrographs of pristine LTO powder (A) and LTO powder heated to 500 °C (B), 600 °C (C), 800 °C (D), 900 °C (E), and 1000 °C (F) under hydrogen atmosphere. The insets show digital photographs of the respective powders with identical mass (0.3 g each).

band (absorption maxima). With increasing treatment temperature, the rising Ti^{3+} content causes the in-gap states to form energy bands which expand in direction of the conduction and valence band simultaneously (i.e., absorption band widens). For highly modified powders, this causes a continuous in-gap band spreading from the band gap into the conduction band or, at the very least, up to 0.5 eV below the conduction band according to the maximum wavelength measurable with our device. Hence, we confirm electron band structures comparable to metals in the strongly modified powders, as electrons can now freely drift due to the coalescence of the occupied “mid-gap bands” and the empty conduction band. This implies a

strong modification of the electrical conductivity for oxygen-deficient samples.

Nitrogen sorption isotherms of the LTO powders show a type II shape, which is typically observed for materials in absence of micro- or mesopores (Figure 3B).^[62] The pristine powder is characterized by a BET specific surface area (SSA) of 25 m²/g and a pore volume of 0.04 cm³/g due to the nanometer-sized primary particles. Only minor changes of the isotherms and corresponding BET specific surface area (SSA; Table 3) are observed for temperatures ≤ 800 °C, which aligns with the morphologies observed with electron microscopy (i.e., microstructure is conserved/absence of sintering). When further increasing the temperature, we see a strong decrease of BET

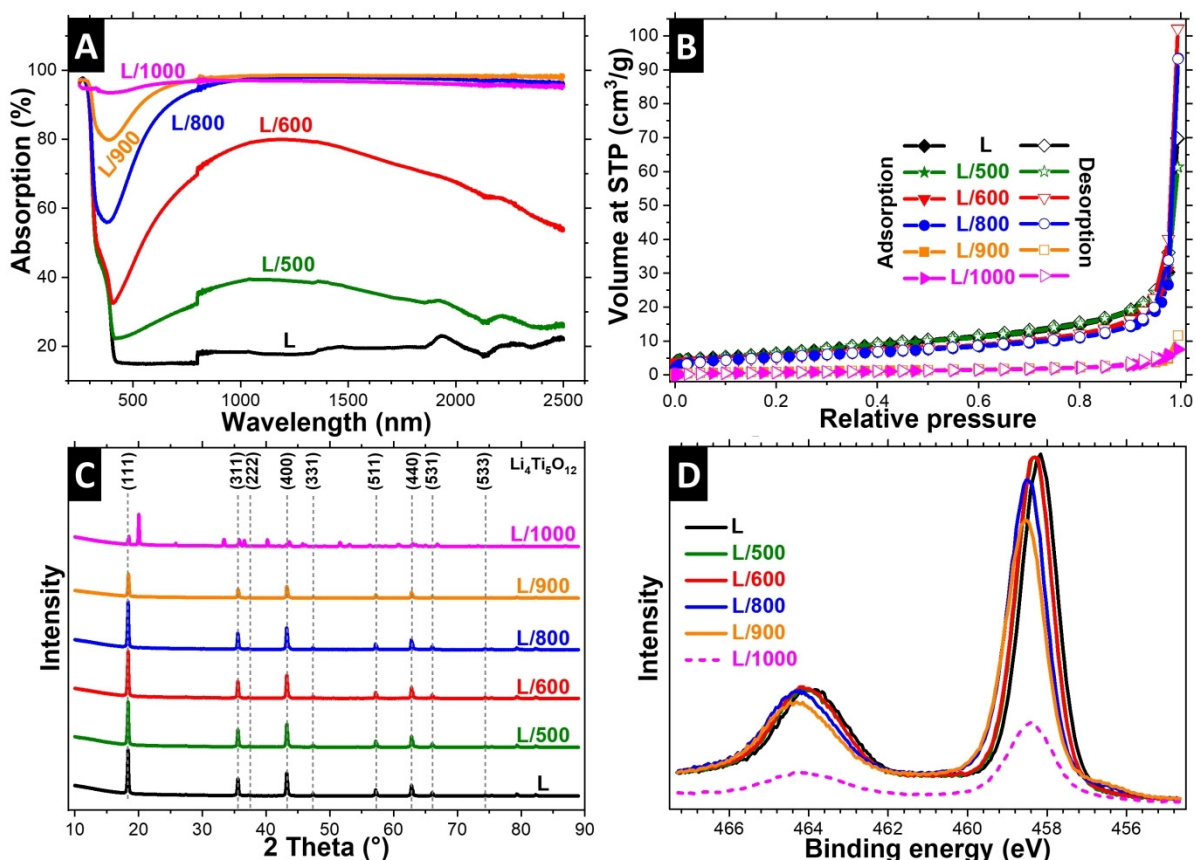


Figure 3. Material characterization of pristine LTO and LTO powder heated to different temperatures under hydrogen atmosphere. UV-VIS-NIR absorption spectra (A), gas sorption isotherms (B), X-ray diffraction pattern with indexed position of spinel $\text{Li}_4\text{Ti}_5\text{O}_{12}$ lattice planes (C), Ti 2p high-resolution XPS-spectra and UV/VIS adsorption spectra (D).

SSA and total pore volume below $4 \text{ m}^2/\text{g}$ and $0.01 \text{ cm}^3/\text{g}$, respectively. This reflects the observed sintering of LTO primary particles and the drastic powder morphology changes of these samples.

X-ray diffraction patterns were recorded (Figure 3C) to examine the crystal structure and crystalline phase content of the LTO powders. Broad signals, coming from spinel LTO (JCPDS 49-0207), and a minor contribution of rutile TiO_2 (JCPDS 21-1276) were detected in the pristine material. The phase distribution of the sample was calculated to 99:1 by mass (LTO/ TiO_2) according to Rietveld refinement of the XRD patterns (Table 4). After hydrogen annealing, an additional monoclinic Li_2TiO_3 (JCPDS 4-009-2812) phase forms and the fraction of spinel LTO and rutile TiO_2 decreases with increasing temperature. The Li_2TiO_3 phase tends to increase with rising temper-

ature, but does not exceed 8 mass% up to 900°C . The LTO crystallinity is largely maintained up to a temperature of 800°C , as deduced from the almost constant XRD signal amongst these samples. For L/900, partial amorphization accompanied by a contraction of the (111) lattice planes takes place as seen from a decrease of the XRD signal intensity decreases and a shift of the (111) reflection to higher diffraction angles, Figure 3C and Figure S1. This supports our hypothesis of a transition of the reaction mechanism during annealing in hydrogen between 800 – 900°C , since the removal of high energy oxygen sites could likely induce the collapse/amorphization of the LTO structure via a distorted crystalline transition state.

Table 3. Specific surface area and pore volume of the pristine and modified LTO powders.		
Sample	BET SSA [m^2/g]	Pore volume [cm^3/g]
L	25	0.04
L/500	24	0.04
L/600	19	0.03
L/800	19	0.03
L/900	4	0.01
L/1000	3	0.01

Table 4. Crystalline phase contents according to Rietveld fitting of the measured X-ray diffraction patterns.

Sample	$\text{Li}_4\text{Ti}_5\text{O}_{12}$ spinel [mass%]	TiO_2 rutile [mass%]	Li_2TiO_3 monoclinic [mass%]	$\text{Li}_{0.57}\text{Ti}_{0.86}\text{O}_2$ ramsdelite [mass%]
L	99	1	n.d. ^[a]	n.d.
L/500	94	1	5	n.d.
L/600	94	1	5	n.d.
L/800	92	< 1	8	n.d.
L/900	92	n.d.	8	n.d.
L/1000	6	n.d.	21	73

[a] n.d.: not detectable.

It is probable that the amorphization causes the abrupt microstructure change for the samples treated at $\geq 900^\circ\text{C}$ due to a higher material diffusivity in the disordered state or even by liquefaction of the amorphous phase at high temperature. When the temperature reaches 1000°C , a phase transformation of LTO mainly to ramsdellite $\text{Li}_{0.57}\text{Ti}_{0.86}\text{O}_2$ (JCPDS 1-070-2365) and some monoclinic Li_2TiO_3 takes place (Figure 3C, Table 4). According to the phase diagrams, LTO starts to decompose at temperatures above $1015 \pm 5^\circ\text{C}$ into ramsdellite $\text{Li}_{0.57}\text{Ti}_{0.86}\text{O}_2$ and monoclinic Li_2TiO_3 .^[77] Hence, the high-temperature phase transformation observed in our case is likely promoted by growing structural instabilities due to the removal of high energy oxygen atoms from the LTO lattice at temperatures above 800°C (Section 2.1.). Initially, this leads to the contraction of the (111) lattice planes with a subsequent amorphization and phase transformation.

XPS survey scans were recorded to calculate the near-surface chemical composition (Table 5). All powders show XPS signals for Li, C, O, and Ti. For the pristine material, the ratio of Li/Ti/O elements is about 1:2:6, which should theoretically be at around 1:1:3 for LTO. The excess amount of Ti and O and its ratio of 1:2 indicates the presence of an additional TiO_2 side phase. According to the XPS elemental chemical composition, the ratio of LTO to TiO_2 is roughly 1:1. This differs from the 99:1 ratio determined by XRD characterization and suggests that the TiO_2 phase is either mainly located in near-surface regions and/or that amorphous TiO_2 is present in the sample, since XPS only probes near-surface regions and XRD solely detects crystalline phases. About 10 atom% of carbon was detected in the surface of the pristine powder. Such values can be caused by surface absorption of impurities from the environment and are commonly observed for samples which were not strictly prepared and stored in ultrahigh vacuum conditions. The near-surface chemical composition is largely maintained for the modified LTO powders treated at temperatures of up to 900°C . For L/1000 an abrupt increase of Li and C is observed, while the Ti amount simultaneously decreases.

All powders show an O 1 s peak centered at about 529.6–529.9 eV (Figure S2A), and a Li 1 s peak at about 54.2–54.7 eV (Figure S2C), which are characteristic binding energies of electrons originating from O respectively Li in metal oxides like LTO.^[65,78] For L/1000, an additional peak arises at 531.7 eV (O 1 s) and at 55.2 eV (Li 1 s), which can be attributed to oxygen and lithium ions in Li_2CO_3 .^[78] This is further supported by the C 1 s peak of L/1000 at 289.9 eV (Figure S2B), which can be assigned

to carboxylic groups.^[79–81] Therefore, the observed change of chemical composition is caused by the formation of a Li_2CO_3 containing phase at the surface of L/1000. While the exact origin of this phase remains unclear, surface precipitation of Li_2CO_3 during the phase transformation or a chemical reaction with ambient CO_2 during sample transfer is conceivable (i.e., caused by the oxophilicity of the highly oxygen-deficient material). A drift of the XPS peaks to higher binding energies with increasing treatment temperature can be seen in all high-resolution XPS spectra, except for the C1s spectra, which was shifted to 285 eV for calibration. It is unlikely that the observed drift is caused by surface charging effects, as it is pronounced to different degrees for the various elements. Several interacting factors could be responsible for the drifting of the XPS peaks: i) elevation of the Fermi-level caused by the high oxygen vacancy concentration, ii) change of chemical environment due to surface phase transformation, and iii) varying degree of near-surface band bending due to contact formation to distinct surface phases (e.g., Li_2TiO_3) and/or surface adsorbates (e.g., O_2 , H_2O or CO_2). Especially latter have been linked to energy band bending phenomena and binding energy drifts in TiO_2 .^[82–84] An adsorption of oxygen-containing species is likely due to the general high oxophilicity of titanium (especially in its reduced state; Ref. [84]) and the high oxygen deficiency of the materials treated at elevated temperatures. This is also supported by the slightly higher mass of high temperature modified powders (L/800, L/900, and L/1000) when compared to the thermogram (Figure 1A). Moreover, the shoulder at 531–533 eV in the O 1 s spectra for the heat-treated powders suggests a rising tendency for oxygen and water absorption (especially recognizable for L/800 and L/900). This shoulder has been connected to hydroxyl groups formed by chemisorption of water and to chemisorbed oxygen on LTO and TiO_2 surfaces.^[65,66]

The Ti 2p high-resolution XPS spectra (Figure 3D) of the LTO powders show the high-intensity $\text{Ti} 2p_{3/2}$ peak centered at 458.2–458.6 eV and a low-intensity $\text{Ti} 2p_{1/2}$ peak at 463.9–464.4 eV. These binding energies are typically observed for tetravalent titanium.^[65,85] The Ti 2p peak intensity of L/1000 is severely decreased due to the arising Li_2CO_3 side phase at this treatment temperature. An additional small shoulder of the $\text{Ti} 2p_{3/2}$ peak emerges for the treated powders at about 455.6–457.1 eV, which can be attributed to trivalent titanium.^[65,85] Both components have been fitted by two separate peaks and the resulting $\text{Ti}^{3+}/\text{Ti}^{4+}$ ratio is provided in Table 5. For peak-fitting, we assumed the Ti^{3+} component for all samples to obtain consistent data. Accordingly, small amounts of Ti^{3+} are also obtained for the pristine sample. We did not identify a significant difference of the $\text{Ti}^{3+}/\text{Ti}^{4+}$ ratio between the pristine material and L/500 respectively L/600, while powders treated at higher temperatures show a minor increase of the Ti^{3+} species. The calculated ratio of the XPS measurements for high-temperature treated samples is lower by a factor of 2–5 compared to the ratio obtained from the TG-MS results (Table 2). Hence, the chemisorption of gaseous species (O_2 , H_2O , or CO_2) during sample transfer results in a near-surface re-oxidation of titanium. However, the bulk vacancy concentration is largely maintained, since reduced LTO is typically stable in air for

Table 5. XPS elemental analysis and calculated ratio of $\text{Ti}^{3+}/\text{Ti}^{4+}$ species of pristine and of the modified LTO powders. The average value and the standard deviation refer to measurements at three different positions.

Material	Li content [atom%]	C content [atom%]	O content [atom%]	Ti content [atom%]	$\text{Ti}^{3+}/\text{Ti}^{4+}$
L	10.9 ± 0.4	12.5 ± 0.3	56.3 ± 0.3	20.2 ± 0.2	0.026
L/500	10.6 ± 0.4	12.4 ± 0.2	56.5 ± 0.3	20.6 ± 0.1	0.024
L/600	10.0 ± 0.8	12.5 ± 0.1	56.8 ± 0.6	20.2 ± 0.2	0.025
L/800	10.2 ± 0.5	13.0 ± 0.3	56.3 ± 0.2	20.1 ± 0.2	0.046
L/900	10.5 ± 1.1	14.2 ± 0.5	56.1 ± 0.5	19.2 ± 0.1	0.062
L/1000	18.3 ± 1.6	18.9 ± 0.9	55.0 ± 0.8	7.1 ± 1.5	0.053

weeks/months.^[56] Accordingly, XPS results must be carefully interpreted for valence-tuned LTO and a shift of 2p X-ray photoelectron spectra, like proposed by Shen et al.,^[57] cannot be seen as evidence for the formation of Ti³⁺ valence states.

Summarizing these data, we see that the bespoke reduction of titanium oxidation state was successfully achieved by a simple and rapid process. It consists of fast heating under hydrogen and subsequent immediate cooling, without the need for time-consuming/cost-ineffective high-temperature holding steps or elaborate high-pressure techniques. This procedure maintains the LTO nanostructure and largely prevents the sintering of particles due to the short timespan in the high temperature regime. When operating in an appropriate temperature range (i.e., $\leq 800^\circ\text{C}$), the titanium oxidation state can be adjusted, while circumventing LTO phase transformations or amorphization.

2.3. Understanding the Rate Limitations of Nanoparticulate Lithium Titanate Electrodes

To enable high power operation of electrochemical energy storage devices, like hybrid supercapacitors, the solid Li-ion transport paths through the active materials need to be minimized, while the electrode/electrolyte interface should be maximized.^[86] This is due to the much higher Li-ion conductivity of the liquid electrolyte as compared to solid-state Li-ion diffusion inside the electrode materials.^[86] From this point of view, nanosizing of the active material is a common and effective approach to resolve this issue. In case of insulating active materials, like Li₄Ti₅O₁₂, this can entail additional challenges with the electrochemical stability, as we have shown recently.^[14] A decreasing particle size of the insulating Li₄Ti₅O₁₂ will reduce the insulating to conductive particle size ratio (conductive carbon size is constant). According to Monte Carlo simulations of He et al.,^[87] a reduction of this ratio will raise the threshold of conductive additive material required for electrical percolation. Hence, nanometer-sized Li₄Ti₅O₁₂ is very effectively disrupting the electrical percolation paths^[14] and the electrical conductivity of a nanopowder may be much more limiting as compared to a powder with a larger particle size. In the case of LTO, this only holds if the low electrical conductivity of the Li-poor phase (Li₄Ti₅O₁₂) is the rate limiting factor and the emerging conductive Li-rich phase (Li₇Ti₅O₁₂) is not sufficient to provide the required electrical percolation during cell operation. In a first step, we will clarify this issue via rate capability assessment of electrodes containing no CB (0-L) and electrodes with 5 mass% respectively 20 mass% CB (5-L respectively 20-L) as state-of-the-art literature on this topic is contradictory (Section 1).

To probe the electrical percolation, electrodes were sandwiched between two titanium pistons, while applying a current and measuring the potential between both pistons. For 0-L and 5-L, a pronounced initial voltage increase, followed by a lower subsequent polarization can be observed (Figure S4A). This polarization indicates that electrical charge is accumulated between both pistons due to the insulating nature of these

electrodes (working principle of a parallel plate capacitor). Accordingly, the carbon concentration for 5-L is not sufficient to reach the percolation threshold. By contrast, for 20-L no polarization was detectable due to the high amount of conductive carbon (i.e., percolation threshold is reached).

The electrochemical rate capability of 0-L, 5-L, and 20-L was normalized to the total LTO mass of the electrode and the corresponding data are shown in Figure 4a. At low rates of 0.1C, the LTO capacity is about 160 mAh/g for 5-L, which is slightly lower as compared to the theoretical value of 175 mAh/g.^[16] Such values are common for commercial materials and can, for example, be caused by small impurities.^[11,56] This implies that almost all active material particles do possess a sufficient electrical contact to the current collector. The slightly smaller values of 0-L are likely connected to a minor amount of electrically insulated particles, while 20-L is about in the statistical scatter range of 5-L results. For 20-L, the electrical percolation is established by the CB matrix. Since 0-L and 5-L are electrical insulating and do not have a CB percolation network, the electrical percolation necessarily must be formed during charging. Electrical percolation is established during lithiation when electrically conductive, Li-rich LTO is being formed.^[14] With increasing the C-rate, the behavior changes and we see significant differences between 0-L, 5-L, and 20-L. In case of carbon-free electrodes, a sharp decline of the LTO capacity is observed and the capacity drops from about 150 mAh/g to 30 mAh/g when raising the charging/discharging rate from 0.1C to 20C. We attribute this to a cascade-like effect which de-activates more and more conductive paths during delithiation when conductive Li-rich phase is being replaced by the insulating Li-poor phase.^[14] At high rates, this process seems to be amplified due to the smaller timescale of one discharge cycle and the associated more inhomogeneous distribution of charge and potential differences throughout the electrode.^[14] Hence, well-connected areas of Li-rich LTO particles will be delithiated at first and the most effective conductive paths are lost shortly after initiation of the discharge.

The rate performance of 5-L is superior to 0-L, although the carbon content of 5-L is not sufficient to provide effective electrical percolation. In this case, the conductive paths are likely co-provided by CB and Li-rich LTO. Therefore, the conductive paths are only partially de-activated during fast de-lithiation as some conductivity can still be maintained by carbon and the conductivity of the Li-rich phase mostly serves to connect certain electrode areas. Cells based on 20-L show superior rate performance as compared to 0-L and 5-L, since electrical percolation is solely established by the conductive carbon network. Hence, the high rate behavior of 20-L is not dictated by the arising Li-poor LTO phase and is limited by intra-particle Li-ion and/or electron conduction kinetics. The differences between 20-L and 5-L are likely connected to the small size of the LTO nanoparticles, since the electrical percolation of conventional micrometer-sized particles is usually already achieved at carbon contents below 5 mass%.^[88–90] From these results, we see that the rate limitation of nanoparticulate LTO based cells is caused by the low conductivity of the Li-poor phase. Only when we remove this rate limitation by increasing the carbon content, this behavior changes and the rate

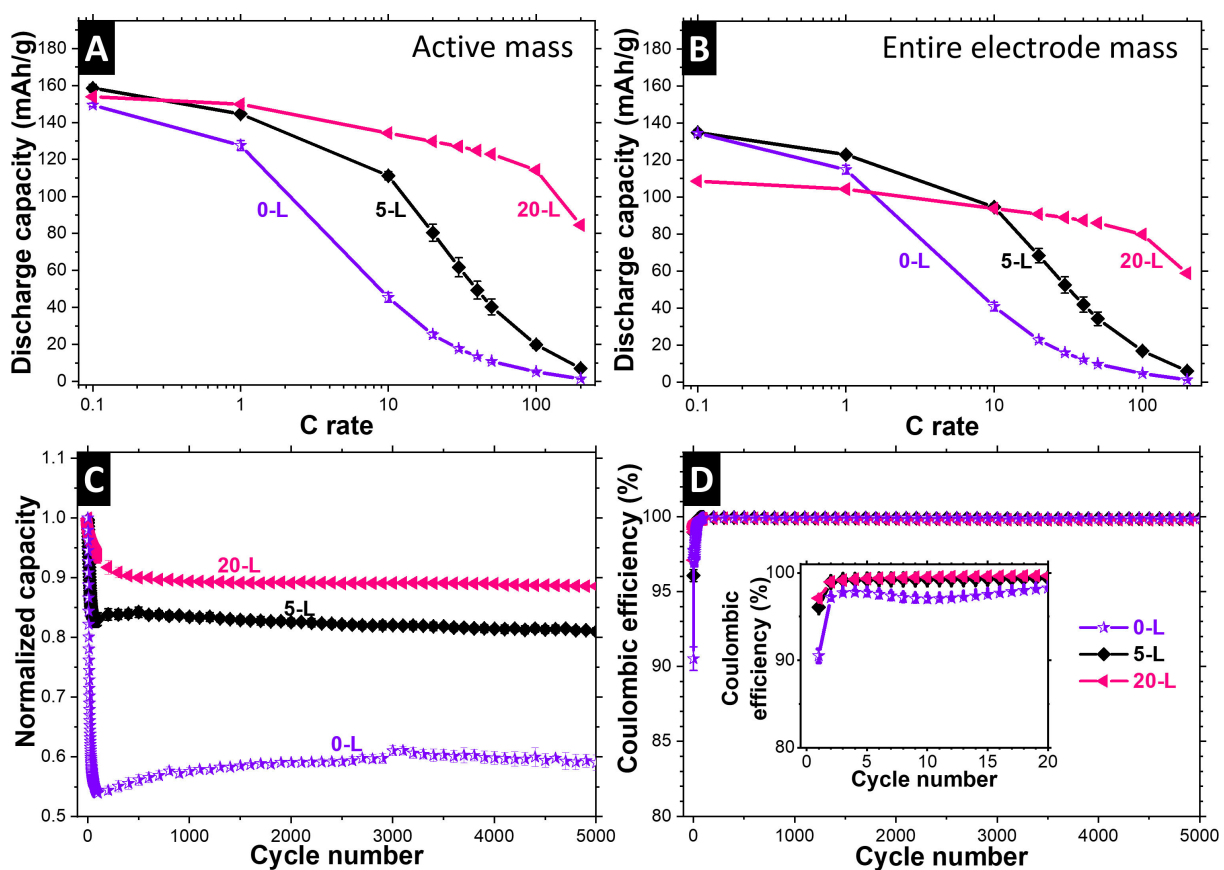


Figure 4. Rate performance based on active or electrode mass (A,B). Electrochemical cycling stability (C) and Coulombic efficiency at charging/discharging rates (D) of 10C of electrodes containing LTO with different carbon concentrations.

capability gets determined by intra-particle conductivity limitations. It is insufficient to only consider the high conductivity of the Li-rich phase to identify the rate limitations of LTO based electrodes,^[25] since the emerging de-lithiated phase can heavily disrupt conduction paths during fast de-lithiation.

Our findings are contradictory to the results to Wang et al. who concluded that “slow ionic transport (not low electronic conductivity) limits the rate performance of $\text{Li}_4\text{Ti}_5\text{O}_{12}$ anodes”^[26]. In this study, the influence of carbon coatings was investigated. Non-coated LTO was found to be superior to coated LTO, although the carbon additive content (10 mass%) of the electrodes was not considered (i.e., carbon concentration might already be sufficient to provide electrical percolation and carbon-coating is redundant). Moreover, from determination of Li-ion diffusion coefficients, the authors concluded that the “carbon layer hinders lithium ion diffusion into the $\text{Li}_4\text{Ti}_5\text{O}_{12}$ lattice” and explains the impaired rate performance.^[26] While this demonstrates that a carbon layer can act as an additional barrier for lithium ion diffusion under certain circumstances, it should not be considered as a general evidence for Li-ion diffusion limitation in LTO based electrodes. Such a conclusion can only be drawn when specifically modifying the intra-particle electrical conductivity without impacting Li-diffusion kinetics. Therefore, our results show that the electrode conductivity can be rate limiting for LTO-based cells, but we cannot

specify if the intra-particle kinetics are either dictated by Li-ion diffusion or by electrical conductivity.

The electrochemical cycling stability at 10C scales with the carbon content (Figure 4C). Lower Coulombic efficiencies are observed during the first cycles of 0-L and 5-L cells. Carbon-free electrodes drop below 60% of the initial capacity already after 30 cycles, while about 90% of the capacity is maintained for 20-L even after 5000 charge/discharge cycles. These findings are consistent with our recent work and likely attributed to local degradation spots caused by inhomogeneous current/voltage distribution throughout the electrode for compositions without carbon or with low carbon content.^[14] We conclude that carbon-free/low carbon content based LTO cells may be suitable for certain low rate applications, but this deteriorates the rate capability and electrochemical stability. The usage of LTO for such applications is questionable considering that these are critical unique selling points of LTO based cells over other anode materials with higher capacity (e.g., Sn, Si, or SiO_2 ; Ref. [91]).

Undoubtedly, a high carbon content greatly improves the electrochemical performance, but it comes at the expense of a decreased overall electrode capacity since carbon is electrochemically inactive in the operating potential of LTO (Figure 4B). This performance is of significantly greater importance for practical application in an electrochemical energy storage device. For such applications, it is not of interest how well a

small quantity of LTO performs in a massive matrix of carbon; the main challenge is to achieve a superior performance with the lowest possible amount of conductive carbon. Therefore, increasing the intrinsic electronic conductivity of LTO is the best solution, as we will show throughout the next section.

2.4. Electrochemical Properties of Modified LTO Powders

The carbon content for all follow-up experiments was kept at 5 mass% since this composition was found to be superior to carbon-free electrodes and yet possess a high capacity with respect to the entire electrode mass. At this carbon concentration, the rate capability remains limited by the low conductive Li-poor phase and an improvement of the intrinsic electrical conductivity of LTO is required for high rate operation.

In case of 5-L/500 and 5-L/600, the low amount of Ti^{3+} valence states did not lead to significant enhancement of the electrical conductivity and the electrode still is electrically insulating (Figure S4B). By contrast, treatment at higher temperatures did lead to massive enhancement of the electrical conductivity, since no polarization was detectable for these electrodes (Figure S4B).

At low charge/discharge rates, the capacity of pristine LTO is maintained for the modified powders L/500, L/600, and L/800 (Figure 5A). This confirms that enough Ti^{4+} is present to attain the full LTO capacity. These species are vital for the LTO redox reaction, as Ti^{4+} is reduced to Ti^{3+} during lithiation to ensure charge neutrality during Li-insertion. The characteristic two-phase lithiation/de-lithiation mechanisms of LTO is preserved for all LTO powders as can be deduced from the flat voltage plateau below 1.6 V vs. Li/Li⁺ (Figure 6A) and the two redox peaks between 1.4–1.7 V vs. Li/Li⁺ of the cyclic voltammograms (Figure 6C).^[92] With increasing treatment temperature, the voltage plateau position seems to be continuously lowered towards small potentials vs. Li/Li⁺ (Figure 6A, inset). A shift of the voltage plateau may be linked to overpotential development due to a deterioration of the redox process kinetics. However, a rising overpotential would simultaneously force the lithiation plateau to lower potentials and the de-lithiation plateau to higher potentials vs. Li/Li⁺.^[14] Since both plateaus are coincidentally shifted to lower polarizations (e.g., about 30 mV for 5-L/900), the half-wave potential (HWP) of the LTO lithiation/de-lithiation reaction seems to be modified for the oxygen-deficient LTO samples. The HWP is correlated to the energy, which is required to insert or remove Li-ions into the active materials.^[93] Since the HWP is shifted to higher polarizations for

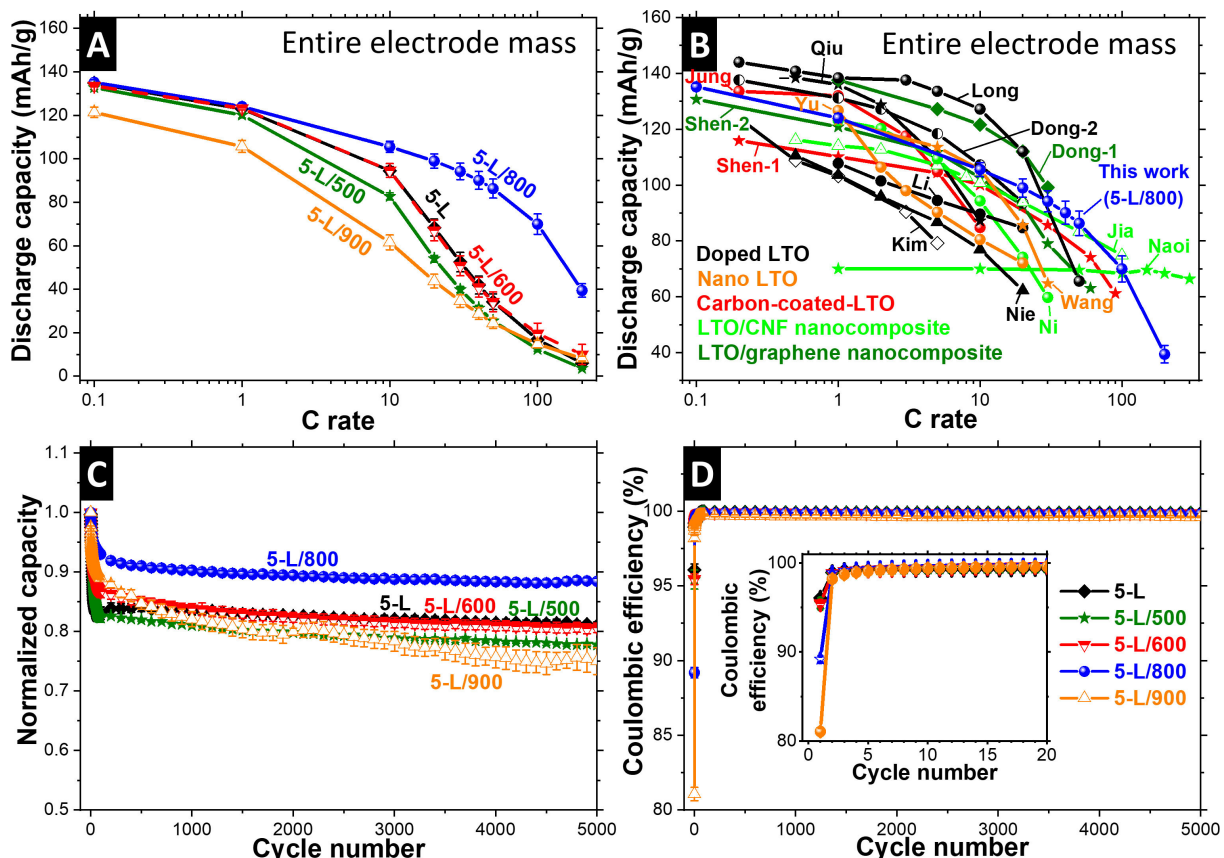


Figure 5. Rate performance (based on electrode mass) (A) including a comparison to literature (B), electrochemical cycling stability (C) and Coulombic efficiency at charging/discharging rates (D) of 10C of electrodes containing modified LTO. The literature values were converted to electrode mass with active mass capacities and electrode composition stated in the respective references (Dong-1,^[38] Dong-2,^[99] Jia,^[28] Jung,^[107] Kim,^[108] Li,^[109] Long,^[110] Naoi,^[17] Ni,^[32] Nie,^[58] Qiu,^[56] Shen-1,^[111] Shen-2,^[112] Wang,^[103] Yu^[113]).

the modified LTO powders, this energy seems to be increased in case of the modified powders. Possibly, this is linked to lattice distortion of the oxygen-deficient samples.^[93] A shifting of the LTO HWP to lower voltages vs. Li/Li⁺ is beneficial for an LTO-based electrochemical energy storage device due to the proportionality of the energy density to the potential. Below 1.3 V vs. Li/Li⁺, a small decrease of the voltage profile slope can be observed (Figure 6A), which may be connected to a minor lithiation beyond $\text{Li}_2\text{Ti}_5\text{O}_{12}$ composition.^[15,94–96] The reaction seems to be strongly influenced by electrochemical kinetics, since it was only observed for low rates of 0.1C (Figure 6A–C). This could be associated to the rising ionic diffusion resistance, which is observed when the Li-rich phase ($\text{Li}_2\text{Ti}_5\text{O}_{12}$) is further lithiated.^[14]

Our data show no additional capacity in the working potential window of LTO for monoclinic Li_2TiO_3 . This is consistent with literature, as monoclinic Li_2TiO_3 has a poor Li-ion storage capacity of about 20 mAh/g.^[97] The latter value would mathematically translate to an additional contribution to the overall electrode capacity of about 1 mAh/g in our case. Since the full capacity of LTO is maintained and the capacity contribution of the Li_2TiO_3 side phase is negligible, we can confirm LTO phase preservation up to treatment temperature of 800 °C. We conclude that emerging crystalline Li_2TiO_3 at low temperatures (800 °C and below) cannot arise from a decomposition of LTO during heat treatment as this should entail a simultaneous capacity decrease. It is likely that the observed rutile TiO_2 phase could react with residual Li_2CO_3 (LTO is usually synthesized by thermal annealing of TiO_2 and Li_2CO_3 ; Ref. [55, 98, 99]) to form Li_2TiO_3 . This would agree with the observed CO_2 release that we measured during thermogravimetric analysis. However, rutile TiO_2 only makes up about 1 mass% of the entire mass of the pristine LTO and no crystalline Li_2CO_3 was detected during XRD characterization. Since the amount of the Li_2TiO_3 side phase is much larger (about 8 mass% for L/800), it must arise from an amorphous phase or phases, which cannot be detected by XRD. Such amorphous phases could decompose or crystallize into monoclinic Li_2TiO_3 after thermal annealing under hydrogen atmosphere at temperatures of 800 °C and below. This hypothesis is supported by the measured capacity of LTO, which is about 92% of its theoretical capacity (i.e., 8 mass% of electrochemically inactive impurity phase might be contained in the pristine LTO). It is reasonable to assume that the amorphous phases are nearly entirely converted into monoclinic Li_2TiO_3 at 800 °C. Hence, the LTO content only seemingly decreases, simply due to the rise of an additional crystalline phase and its impact on the phase distribution. Based on the entire mass (amorphous and crystalline), the LTO content remains constant. The capacity for electrodes based on 5-L/900 is decreased by about 12 mAh/g, likely caused by the partial LTO amorphization, the contraction of the (111) lattice planes, and/or related to the drastic changes of the particle morphology.

The reversible capacity of 5-L/1000 is further decreased to about 90 mAh/g at low rates (Figure S3), which is related to the high-temperature phase transformation of LTO into Li_2TiO_3 and $\text{Li}_{0.57}\text{Ti}_{0.86}\text{O}_2$. In this case, the capacity is mainly accomplished by

the $\text{Li}_{0.57}\text{Ti}_{0.86}\text{O}_2$ phase as the LTO content in the electrode and the charge storage capabilities of Li_2TiO_3 are negligible. According to literature (e.g., Ref.^[100]), $\text{Li}_{0.57}\text{Ti}_{0.86}\text{O}_2$ can reversibly store about 150 mAh/g, which translates to 130 mAh/g normalized to the electrode mass in our case. The capacity difference may originate from an incomplete phase transformation with electrochemically inactive amorphous phases and/or large particles. According to Tsuyumoto et al.,^[101] the black color and the two differently sloped areas during galvanostatic charging (Figure S3B) are characteristic for the oxidized ramsdellite-type lithium titanate ($\text{Li}_{0.5}\text{TiO}_2$). However, 5-L/1000 electrodes show

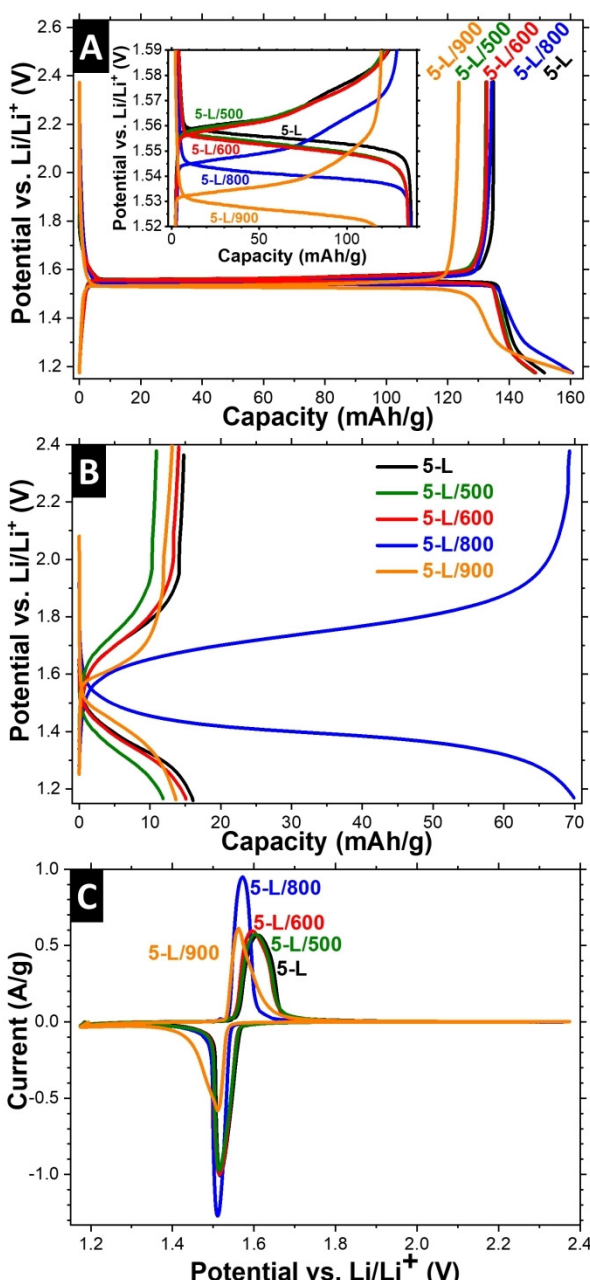


Figure 6. Galvanostatic charge and discharge curves normalized to electrode mass of the 3rd cycle measured at 0.1C (A) and at 100C (B). Cyclic voltammograms recorded with 0.1 mV/s (C). The inset of (A) shows a higher magnification of the lithiation/de-lithiation plateau of LTO at 0.1C.

an inferior rate capability due to the high amount of Li_2TiO_3 and the large active material particle size of this sample. Hence this material is not suitable for high power applications and was not further investigated.

At high rates, the capacity initially decreases for the weakly modified sample 5-L/500, is restored for 5-L/600, reaches an optimum for 5-L/800, and is diminished for 5-L/900 (Figure 5A). This behavior suggests that an impaired Li-diffusion must arise with increasing treatment temperature, as the electrical conductivity is tendentially increased due the rising Ti^{3+} concentration. Since the surface area and powder morphology is barely altered at temperatures $\leq 800^\circ\text{C}$, this decreasing Li-diffusion kinetic must be related to the emerging Li_2TiO_3 phase and the associated decreasing fraction of rutile and/or amorphous TiO_2 . In fact, small amounts of anatase or rutile TiO_2 impurity phases are known to beneficially impact the rate performance of LTO.^[102,103] Moreover, monoclinic Li_2TiO_3 is a poor Li-ion conductor^[104,105] and its presence likely also deteriorates the cell performance. For 5-L/500, the aggravation of Li-ion diffusion outweighs the minor increase of electrical conductivity and the overall rate performance declines. When increasing the treatment temperature, the Li_2TiO_3 content does only marginally change, whereas the $\text{Ti}^{3+}/\text{Ti}^{4+}$ ratio and the associated electrical conductivity gradually rises. Hence, the gain in electrical conductivity first compensates (5-L/600) and then outweighs (5-L/800) the diminishing Li-ion diffusion kinetics after heat treatment. In case of 5-L/900, the abrupt change of particle microstructure further decreases the Li-diffusion kinetics. An increased particle size and the simultaneous decreased electrode/electrolyte interface area lead to increased solid Li-ion diffusion lengths and the positive effect of electrical conductivity is outweighed. At ultra-high C-rates of 100C, a capacity of about 70 mAh/g is maintained for 5-L/800, whereas all other samples with equal carbon contents only deliver capacities of around 15 mAh/g (Figure 6B). These superior electrochemical kinetics of 5-L/800 can also be deduced from the sharp redox peaks observed during cyclic voltammetry measurements (Figure 6C).

While powders treated at 500°C , 600°C , and 900°C are comparable to the pristine sample, a strong improvement of the cycling stability is achieved for 5-L/800 (Figure 5C). For this electrode, about 90% of the initial capacity is remained after 5000 charge/discharge cycles at 10C, which is like electrodes containing excessive amounts of carbon (20-L). The capacity decay pattern is almost identical for 5-L/800 and 20-L as both electrodes show a pronounced declining capacity during the first cycles and an almost constant capacity for the subsequent cycles. This is related to the increased fraction of $\text{Ti}^{3+}/\text{Ti}^{4+}$ and the associated increase of electrical conductivity of the delithiated phase. Furthermore, the increased amount of oxygen vacancies and titanium with Ti^{3+} valence state does not alter the electrochemical stability of the cells. Since these arguments are also valid for 5-L/900, the presence of the amorphous phase or structural instabilities during cycling caused by the contracted (111) lattice planes explain the inferior stability of this sample. For the slightly modified powders L/500 and L/600, the fraction of $\text{Ti}^{3+}/\text{Ti}^{4+}$ is too small to strongly

increase the electrical conductivity and these samples show a similar cycling behavior as the pristine powder. The Coulombic efficiency decreases when using a higher annealing temperature, for the first cycle and then stabilizes for the subsequent cycles (Figure 5D). This behavior cannot be caused by inhomogeneous current or voltage distribution, as the conductivity of the modified powders is generally higher than of the pristine material, and the latter exhibits a low Coulombic efficiency during all 20 initial cycles (0-L in Figure 4D and Ref. [14]). We therefore ascribe the low first cycle efficiencies to the reduction surface adsorbates on the modified powders. Physisorbed water or OH-species found on the modified LTO powders (Section 2.2) could be reduced to hydrogen.^[3] The declining Coulombic efficiency, when elevating the treatment temperature, is connected to an increasing amount of surface absorbates. This reduction only occurs during the first cycle, without any impact on the subsequent cycles and the beneficial influence of the improved electrical conductivity outweighs this effect by far. Thereby, a superior cycling stability of 5-L/800 results.

Electrodes based on 5-L/800 compositions possess a similar high-power capability and electrochemical cycling stability as compared to electrodes prepared with excessive amounts of conductive carbon. Simultaneously, the overall electrode capacity can be increased by 24% due the reduced amount of conductive carbon. The superior performance relates to the increased ratio of $\text{Ti}^{3+}/\text{Ti}^{4+}$ and the associated high electrical conductivity of the de-lithiated phase. Hydrogen treated LTO challenges state-of-the-art LTO-carbon nanocomposites, especially at high C-rates above 50C (Figure 5B). This is mainly attributed to the increased electrical conductivity and the enabling of high rate capabilities at simultaneously low carbon concentration.

2.5. Performance of Hybrid Supercapacitors with Oxygen-Deficient LTO

The superior electrochemical performance of 5-L/800 electrodes was further demonstrated in a hybrid supercapacitor full-cell setup. We employed an AC-LMO composite cathode to adapt to the ultra-high rate capability and high electrode capacity of the anode. The active mass was set to 65 mass% AC and 35 mass% LMO to obtain equal shares of charge stored via fast ion electrosorption at the AC surface and via high capacitive Faradaic reactions of LMO. To operate both electrodes within the stability window of the electrolyte, the anode/cathode mass ratio was adjusted to 0.37. Accordingly, charging the cell to 2.8 V corresponds to a potential of 4.2 V respectively 1.4 V vs. Li/Li^+ for the cathode and anode, respectively (Figure 7A). The potential profile of the anode shows a voltage plateau at about 1.6 V vs. Li/Li^+ caused by the two-phase reaction of LTO,^[92] while the cathode is characterized by two linear regions with distinct slope. The voltage profile of a composite electrode is a superposition of AC and LMO contributions: For voltages below 3.9 V vs. Li/Li^+ the charge is solely stored via ion electrosorption at the interface of an electrolyte and AC, whereas at 3.9–4.2 V

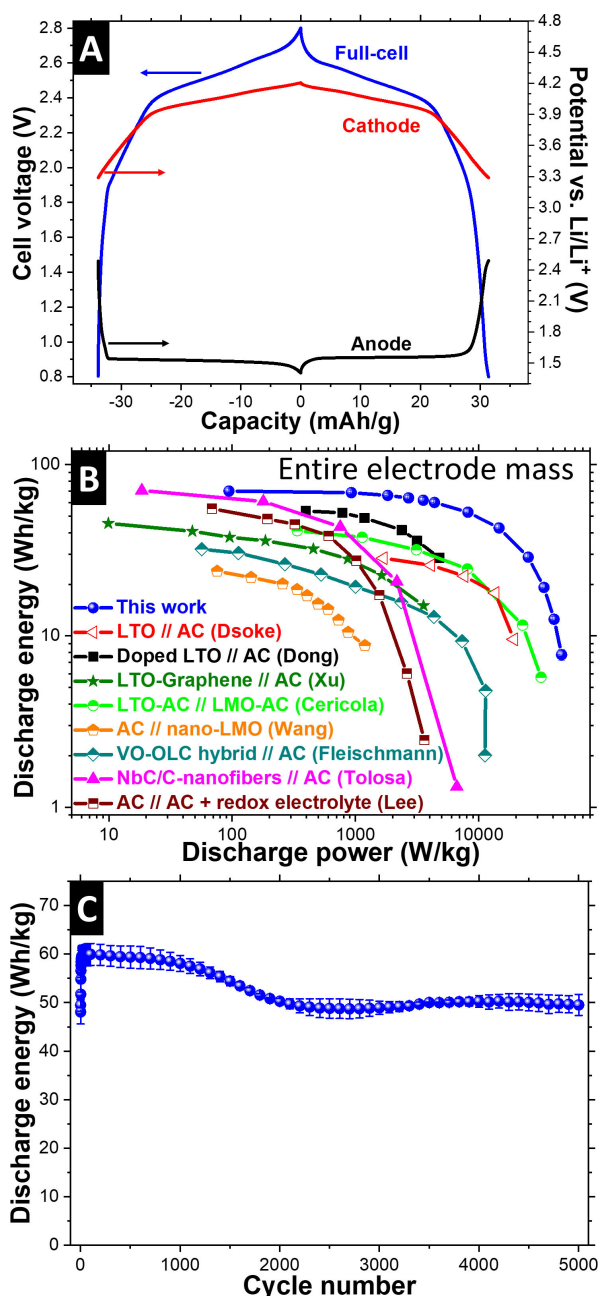


Figure 7. Galvanostatic charge and discharge curves at 1 C, including the voltage profiles of anode and cathode measured against a spectator QRE (A). Ragone-plot with comparison to literature (B). Electrochemical cycling stability at charging/discharging rates of 10C of full-cells employing 5-L/800 anodes and activated carbon/LMO composite cathodes normalized to the entire electrode mass (C). The literature values were converted to electrode mass with active mass energy/power density and electrode composition stated in the respective references (Cericola,^[10] Dong,^[99] Dsoke,^[114] Fleischmann,^[115] Lee,^[116] Tolosa,^[117] Wang,^[118] Xu^[40]).

vs. Li/Li⁺, we also must consider Faradaic charge storage of LMO and associated Li-ion extraction/insertion.

We also calculated the gravimetric energy and power density of the hybrid supercapacitor from GCPL discharge curves at various rates (g⁻¹). The device is characterized by a high energy density of 70 Wh/kg and an ultra-high maximum power density of 47 kW/kg. These values correspond to 82 Wh/

kg and 55 kW/kg based on active mass of both electrodes. About half of the energy can still be maintained, even when operating the cell with a high power of 20 kW/kg. To the best of our knowledge, such a remarkable combination of high power and energy density have not been reported for 3 V devices so far. Especially in the high-power region above 10 kW/kg this cell concept is superior to other hybrid devices described in literature (Figure 7B).

During GCPL, the initial discharge energy increases during the first 60 cycles (Figure 7C). This behavior must be connected to processes taking place at the cathode, since it did not occur for LTO half-cells. Zhang et al. recently reported that the capacity of AC can increase during cycling in an Li-containing electrolyte.^[106] Since we also observed similar effects for AC, it is likely that the initial energy increase is attributed to the AC contained in our cathodes. About 83% of the maximum energy density is maintained after 5000 continuous charge-discharge cycles at charging/discharging rates of 10C and 100% depth of discharge. When increasing the rate to 100C, the device maintains 78% of the maximum energy after 15000 cycles (Figure S5). Such a behavior is typically observed for high rates, since the time spent in the high polarization regime is lower (per cycle) when increasing the charge/discharge rate.^[14] These outstanding device performances underpin the superior electrochemical performance of 5-L/800 electrodes and are a result of: i) Optimized LTO hydrogen treatment conditions, ii) high active mass content of the electrodes, iii) lowering of the LTO plateau positions, and iv) an AC-LMO composite cathode which is well-adjusted to the ultra-high rate capability of the anode.

3. Conclusions

We have increased the Ti³⁺/Ti⁴⁺ ratio of a commercial lithium titanate (LTO) nanopowder through thermal annealing in hydrogen atmosphere. At atmospheric pressure and temperatures above 450 °C, the mass loss and simultaneous water desorption was correlated to the formation of oxygen vacancies and an associated reduction of titanium valence states from Ti⁴⁺ into Ti³⁺. This process leads to massive modifications of the optical properties as the powder changes its color from white first to blue and finally to black. The color change is a result of in-gap energy levels caused by oxygen vacancy formation and associated Ti³⁺ valence states. These energy levels initially occur at about 1 eV below the conduction band and transform to in-gap bands, which spread into the conduction band for highly modified powders. Hence electrons can freely drift due to the coalescence of the occupied “mid-gap bands” with the empty conduction band and the intrinsic electronic conductivity of LTO is considerably increased.

The particle morphology, surface area, crystallinity, and the LTO phase content is largely maintained for annealing up to 800 °C as confirmed by SEM, TEM, gas sorption, and XRD characterization. When further increasing the temperature, the powder density decreases as the LTO nanoparticles initially start to coalesce to larger primary particles at 900 °C and finally transform into micrometer-large particles at 1000 °C. These

processes are accompanied by partial sample amorphization via a distorted crystalline transition state and LTO phase transformation. We have demonstrated that fast heating of nanoparticulate LTO under hydrogen (10 °C/min) to 800 °C and subsequent immediate cooling is sufficient to obtain appropriate Ti³⁺/Ti⁴⁺ ratios. This procedure maintains the LTO structure, prevents the sintering of LTO nanoparticles due to the short timespan in the high temperature regime and does not require any additional high-temperature holding steps or elaborate high-pressure techniques. The associated increase of the intrinsic electrical conductivity of LTO allows us to operate LTO electrodes at C-rates above 50C with a minimal carbon concentration of 5 mass%. Such electrodes are highly competitive to elaborate state-of-the-art LTO-carbon nanocomposites and can deliver a high electrode capacity of about 70 mAh/g (82 mAh/g based on active mass) at ultra-high rates of 100C. Pristine LTO electrodes, on the other hand, are impaired by the low electronic conductivity of the Li-poor LTO phase and therefore require large amounts of electrochemically inactive conductive carbon (20 mass%).

The superior performance of hydrogen treated LTO was further demonstrated in a hybrid supercapacitor full-cell set up against an activated carbon/lithium manganese oxide composite electrode. This device is characterized by an outstanding energy and power density of 70 Wh/kg respectively 47 kW/kg (82 Wh/kg respectively 55 kW/kg based on active mass) and a high electrochemical cycling stability over 5000 charge-discharge cycles (78% after 15000 cycles at 100C).

Acknowledgements

The authors thank C. Engel, A. Fuchs, M. Tuchen, I. Wöhrl, C. Müller, M. Wessling, and A. Böhme for the support and helpful discussions. We acknowledge funding from the German Federal Ministry for Economic Affairs and Energy (BMWi) in support of the HyBaCap project (award number 03ET6113C) and thank Prof. E. Arzt (INM) for his continuing support. We thank M. Zeiger for his help with transmission electron microscopy and B. Krüner for his support with gas sorption analysis (both at INM).

Conflict of Interest

The authors declare no conflict of interest.

Keywords: lithium titanate • lithium ion battery • electrochemical energy storage • hybrid supercapacitor

- [1] Z. Yang, J. Zhang, M. C. W. Kintner-Meyer, X. Lu, D. Choi, J. P. Lemmon, J. Liu, *Chem. Rev.* **2011**, *111*, 3577–3613.
- [2] B. Scrosati, J. Garche, *J. Power Sources* **2010**, *195*, 2419–2430.
- [3] F. Beguin, V. Presser, A. Balducci, E. Frackowiak, *Adv. Mater.* **2014**, *26*, 2219–2251.
- [4] M. Salanne, B. Rotenberg, K. Naoi, K. Kaneko, P. L. Taberna, C. P. Grey, B. Dunn, P. Simon, *Nat. Energy* **2016**, *1*, 16070.

- [5] G. G. Amatucci, F. Badway, A. Du Pasquier, T. Zheng, *J. Electrochem. Soc.* **2001**, *148*, A930–A939.
- [6] N. Böckenfeld, R. S. Kühnel, S. Passerini, M. Winter, A. Balducci, *J. Power Sources* **2011**, *196*, 4136–4142.
- [7] N. Böckenfeld, T. Placke, M. Winter, S. Passerini, A. Balducci, *Electrochim. Acta* **2012**, *76*, 130–136.
- [8] D. Cericola, P. W. Ruch, R. Kötz, P. Novák, A. Wokaun, *Electrochim. Commun.* **2010**, *12*, 812–815.
- [9] D. Cericola, P. Novák, A. Wokaun, R. Kötz, *Electrochim. Acta* **2011**, *56*, 1288–1293.
- [10] D. Cericola, P. Novák, A. Wokaun, R. Kötz, *J. Power Sources* **2011**, *196*, 10305–10313.
- [11] D. Cericola, P. Novák, A. Wokaun, R. Kötz, *Electrochim. Acta* **2011**, *56*, 8403–8411.
- [12] B. Wang, Q. Wang, B. Xu, T. Liu, D. Wang, G. Zhao, *RSC Adv.* **2013**, *3*, 20024–20033.
- [13] M. Secchiaroli, R. Marassi, M. Wohlfahrt-Mehrens, S. Dsoke, *Electrochim. Acta* **2016**, *219*, 425–434.
- [14] M. Widmaier, N. Jäckel, M. Zeiger, M. Abuzarli, C. Engel, L. Bommer, V. Presser, *Electrochim. Acta* **2017**, *247*, 1006–1018.
- [15] W. J. H. Borghols, M. Wagelmaker, U. Lafont, E. M. Kelder, F. M. Mulder, *J. Am. Chem. Soc.* **2009**, *131*, 17786–17792.
- [16] T. Ohzuku, A. Ueda, N. Yamamoto, *J. Electrochem. Soc.* **1995**, *142*, 1431–1435.
- [17] K. Naoi, S. Ishimoto, Y. Isobe, S. Aoyagi, *J. Power Sources* **2010**, *195*, 6250–6254.
- [18] C. H. Chen, J. T. Vaughney, A. N. Jansen, D. W. Dees, A. J. Kahaian, T. Goacher, M. M. Thackeray, *J. Electrochem. Soc.* **2001**, *148*, A102–A104.
- [19] S. Scharner, W. Weppner, P. Schmid-Beurmann, *J. Electrochim. Soc.* **1999**, *146*, 857–861.
- [20] M. S. Song, A. Benayad, Y. M. Choi, K. S. Park, *Chem. Commun.* **2012**, *48*, 516–518.
- [21] C. Kim, Y.-S. Yu, B. Moyon, C. Sirisopanaporn, T. J. Richardson, J. Cabana, *J. Phys. Chem. C* **2016**, *120*, 29030–29038.
- [22] E. Pohjalainen, J. Kallioinen, T. Kallio, *J. Power Sources* **2015**, *279*, 481–486.
- [23] C. Kim, N. S. Norberg, C. T. Alexander, R. Kostecki, J. Cabana, *Adv. Funct. Mater.* **2013**, *23*, 1214–1222.
- [24] C. T. Alexander, C. Kim, R. Yaylian, J. Cabana, *Energy Technol.* **2014**, *2*, 383–390.
- [25] D. Young, A. Ransil, R. Amin, Z. Li, Y.-M. Chiang, *Adv. Energy Mater.* **2013**, *3*, 1125–1129.
- [26] J. Wang, H. Zhao, Z. Li, Y. Wen, Q. Xia, Y. Zhang, G. Yushin, *Adv. Mater. Interfaces* **2016**, *3*, 1600003.
- [27] E. Zhao, C. Qin, H.-R. Jung, G. Berdichevsky, A. Nese, S. Marder, G. Yushin, *ACS Nano* **2016**, *10*, 3977–3984.
- [28] X. Jia, Y. Kan, X. Zhu, G. Ning, Y. Lu, F. Wei, *Nano Energy* **2014**, *10*, 344–352.
- [29] X. Meng, J. Liu, X. Li, M. N. Banis, J. Yang, R. Li, X. Sun, *RSC Adv.* **2013**, *3*, 7285–7288.
- [30] J. Shu, L. Hou, R. Ma, M. Shui, L. Shao, D. Wang, Y. Ren, W. Zheng, *RSC Adv.* **2012**, *2*, 10306–10309.
- [31] J.-H. Choi, W.-H. Ryu, K. Park, J.-D. Jo, S.-M. Jo, D.-S. Lim, I.-D. Kim, *Sci. Rep.* **2014**, *4*, 7334.
- [32] H. Ni, L.-Z. Fan, *J. Power Sources* **2012**, *214*, 195–199.
- [33] K. Naoi, *Fuel Cells* **2010**, *10*, 825–833.
- [34] K. Naoi, S. Ishimoto, J.-i. Miyamoto, W. Naoi, *Energy Environ. Sci.* **2012**, *5*, 9363–9373.
- [35] K. Naoi, W. Naoi, S. Aoyagi, J.-i. Miyamoto, T. Kamino, *Accounts Chem. Res.* **2013**, *46*, 1075–1083.
- [36] Y. Tang, Y. Zhang, X. Rui, D. Qi, Y. Luo, W. R. Leow, S. Chen, J. Guo, J. Wei, W. Li, J. Deng, Y. Lai, B. Ma, X. Chen, *Adv. Mater.* **2016**, *28*, 1567–1576.
- [37] H.-p. Liu, G.-w. Wen, S.-f. Bi, C.-y. Wang, J.-m. Hao, P. Gao, *Electrochim. Acta* **2016**, *192*, 38–44.
- [38] H.-Y. Dong, Y.-B. He, B. Li, C. Zhang, M. Liu, F. Su, W. Lv, F. Kang, Q.-H. Yang, *Electrochim. Acta* **2014**, *142*, 247–253.
- [39] J. Zhu, R. Duan, Y. Zhang, J. Zhu, *Ceram. Int.* **2016**, *42*, 334–340.
- [40] N. Xu, X. Sun, X. Zhang, K. Wang, Y. Ma, *RSC Adv.* **2015**, *5*, 94361–94368.
- [41] C. Lin, B. Ding, Y. Xin, F. Cheng, M. O. Lai, L. Lu, H. Zhou, *J. Power Sources* **2014**, *248*, 1034–1041.
- [42] W. Wang, B. Jiang, W. Xiong, Z. Wang, S. Jiao, *Electrochim. Acta* **2013**, *114*, 198–204.

- [43] H. Duan, J. Li, H. Du, S. W. Chiang, C. Xu, W. Duan, F. Kang, *J. Phys. Chem. C* **2015**, *119*, 5238–5245.
- [44] P. Reale, S. Panero, F. Ronci, V. Rossi Albertini, B. Scrosati, *Chem. Mater.* **2003**, *15*, 3437–3442.
- [45] C. Lin, G. Liang, J. Gao, S. Deng, S. Lin, J. Li, *Functional Materials Letters* **2015**, *09*, 1650012.
- [46] G.-H. Dong, H.-J. Liu, L. Zhou, L. Chong, J. Yang, Y.-M. Qiao, D.-H. Zhang, *J. Alloys Compd.* **2014**, *615*, 817–824.
- [47] S. Sharmila, B. Senthilkumar, V. D. Nithya, K. Vediappan, C. W. Lee, R. K. Selvan, *J. Phys. Chem. Solids* **2013**, *74*, 1515–1521.
- [48] J. S. Park, S.-H. Baek, Y. Park, J. H. Kim, *J. Korean Phys. Soc.* **2014**, *64*, 1545–1549.
- [49] M. Guo, S. Wang, L.-X. Ding, C. Huang, H. Wang, *J. Power Sources* **2015**, *283*, 372–380.
- [50] Z. Yu, X. Zhang, G. Yang, J. Liu, J. Wang, R. Wang, J. Zhang, *Electrochim. Acta* **2011**, *56*, 8611–8617.
- [51] A. F. Orlukas, K. Z. Fung, V. Venckutė, V. Kazlauskienė, J. Miškinis, M. Lelis, *Solid State Ionics* **2015**, *271*, 34–41.
- [52] Q. Zhang, H. Lu, H. Zhong, X. Yan, C. Ouyang, L. Zhang, *J. Mater. Chem. A* **2015**, *3*, 13706–13716.
- [53] T. Yuan, Z. Tan, C. Ma, J. Yang, Z.-F. Ma, S. Zheng, *Adv. Energy Mater.* **2017**, *7*, 1601625.
- [54] J.-Y. Shin, J. H. Joo, D. Samuelis, J. Maier, *Chem. Mater.* **2012**, *24*, 543–551.
- [55] J. Wolfenstine, U. Lee, J. L. Allen, *J. Power Sources* **2006**, *154*, 287–289.
- [56] J. Qiu, C. Lai, E. Gray, S. Li, S. Qiu, E. Strounina, C. Sun, H. Zhao, S. Zhang, *J. Mater. Chem. A* **2014**, *2*, 6353.
- [57] L. Shen, E. Uchaker, X. Zhang, G. Cao, *Adv. Mater.* **2012**, *24*, 6502–6506.
- [58] S. Nie, C. Li, H. Peng, G. Li, K. Chen, *RSC Adv.* **2015**, *5*, 23278–23282.
- [59] M. Widmaier, B. Krüner, N. Jäckel, M. Aslan, S. Fleischmann, C. Engel, V. Presser, *J. Electrochem. Soc.* **2016**, *163*, A2956–A2964.
- [60] D. Weingarth, M. Zeiger, N. Jäckel, M. Aslan, G. Feng, V. Presser, *Adv. Energy Mater.* **2014**, *4*, 1400316.
- [61] S. Brunauer, P. H. Emmett, E. Teller, *J. Am. Chem. Soc.* **1938**, *60*, 309–319.
- [62] M. Thommes, K. Kaneko, A. V. Neimark, J. P. Olivier, F. Rodriguez-Reinoso, J. Rouquerol, K. S. W. Sing, *Pure Appl. Chem.* **2015**, *87*, 1051–1069.
- [63] M. A. Henderson, *Surf. Sci.* **1998**, *400*, 203–219.
- [64] M. B. Hugenschmidt, L. Gamble, C. T. Campbell, *Surf. Sci.* **1994**, *302*, 329–340.
- [65] W. Meng, Y. Xu, B. Yan, J. Guo, *Ionics* **2017**, DOI:10.1007/s11581-017-2278-4.
- [66] G. Li, J. Li, G. Li, G. Jiang, *J. Mater. Chem. A* **2015**, *3*, 22073–22080.
- [67] X.-P. Wang, Y. Yu, X.-F. Hu, L. Gao, *Thin Solid Films* **2000**, *371*, 148–152.
- [68] D. G. Kellerman, N. A. Mukhina, N. A. Zhuravlev, M. S. Valova, V. S. Gorshkov, *Phys. Solid State* **2010**, *52*, 459–464.
- [69] C. Y. Ouyang, Z. Y. Zhong, M. S. Lei, *Electrochim. Commun.* **2007**, *9*, 1107–1112.
- [70] D. Liu, C. Ouyang, J. Shu, J. Jiang, Z. Wang, L. Chen, *physica status solidi b* **2006**, *243*, 1835–1841.
- [71] T. Kostlánová, J. Dědeček, P. Krtík, *Electrochim. Acta* **2007**, *52*, 1847–1856.
- [72] H. Ge, H. Tian, H. Song, D. Liu, S. Wu, X. Shi, X. Gao, L. Lv, X.-M. Song, *Mater. Res. Bull.* **2015**, *61*, 459–462.
- [73] Y.-R. Jhan, J.-G. Duh, *Electrochim. Acta* **2012**, *63*, 9–15.
- [74] Y. Aiura, Y. Nishihara, Y. Haruyama, T. Komeda, S. Kodaira, Y. Sakisaka, T. Maruyama, H. Kato, *Physica B: Condensed Matter* **1994**, *194–196*, 1215–1216.
- [75] X. Chen, L. Liu, P. Y. Yu, S. S. Mao, *Science* **2011**, *331*, 746.
- [76] S.-T. Myung, M. Kikuchi, C. S. Yoon, H. Yashiro, S.-J. Kim, Y.-K. Sun, B. Scrosati, *Energ Environ Sci* **2013**, *6*, 2609–2614.
- [77] G. Izquierdo, A. R. West, *Mater. Res. Bull.* **1980**, *15*, 1655–1660.
- [78] J. F. Moulder, W. F. Stickle, P. E. Sobol, K. D. Bomben, *Handbook of X Ray Photoelectron Spectroscopy: A Reference Book of Standard Spectra for Identification and Interpretation of XPS Data* (Physical Electronics, Eden Prairie, **1995**).
- [79] C. Moreno-Castilla, M. V. López-Ramón, F. Carrasco-Marín, *Carbon* **2000**, *38*, 1995–2001.
- [80] U. Zielke, K. J. Hüttinger, W. P. Hoffman, *Carbon* **1996**, *34*, 983–998.
- [81] Z. R. Yue, W. Jiang, L. Wang, S. D. Gardner, C. U. Pittman Jr., *Carbon* **1999**, *37*, 1785–1796.
- [82] U. Diebold, *Surf. Sci. Rep.* **2003**, *48*, 53–229.
- [83] R. L. Kurtz, R. Stock-Bauer, T. E. Msdey, E. Román, J. De Segovia, *Surf. Sci.* **1989**, *218*, 178–200.
- [84] A. L. Linsebigler, G. Lu, J. T. Yates, *Chem. Rev.* **1995**, *95*, 735–758.
- [85] W. Göpel, J. A. Anderson, D. Frankel, M. Jaehnig, K. Phillips, J. A. Schäfer, G. Rocker, *Surf. Sci.* **1984**, *139*, 333–346.
- [86] P. V. Braun, J. Cho, J. H. Pikul, W. P. King, H. Zhang, *Curr. Opin. Solid State Mater. Sci.* **2012**, *16*, 186–198.
- [87] D. He, N. N. Ekere, *J. Phys. D* **2004**, *37*, 1848.
- [88] G. Liu, H. Zheng, A. S. Simens, A. M. Minor, X. Song, V. S. Battaglia, *J. Electrochem. Soc.* **2007**, *154*, A1129–A1134.
- [89] R. Dominko, M. Gaberšček, J. Drofenik, M. Bele, J. Jamnik, *Electrochim. Acta* **2003**, *48*, 3709–3716.
- [90] R. Dominko, M. Gaberšček, J. Drofenik, M. Bele, S. Pejovnik, *Electrochim. Solid-State Lett.* **2001**, *4*, A187–A190.
- [91] A. Tolosa, M. Widmaier, B. Krüner, J. M. Griffin, V. Presser, *Sustainable Energy & Fuels* **2018**, *2*, 215–228.
- [92] X. Lu, L. Zhao, X. He, R. Xiao, L. Gu, Y.-S. Hu, H. Li, Z. Wang, X. Duan, L. Chen, J. Maier, Y. Ikuhara, *Adv. Mater.* **2012**, *24*, 3233–3238.
- [93] C. Liu, Z. G. Neale, G. Cao, *Mater. Today* **2016**, *19*, 109–123.
- [94] H. Ge, N. Li, D. Li, C. Dai, D. Wang, *Electrochim. Commun.* **2008**, *10*, 719–722.
- [95] X. L. Yao, S. Xie, H. Q. Nian, C. H. Chen, *J. Alloys Compd.* **2008**, *465*, 375–379.
- [96] D. Ahn, X. Xiao, *Electrochim. Commun.* **2011**, *13*, 796–799.
- [97] Y. Wang, A. Zhou, X. Dai, L. Feng, J. Li, J. Li, *J. Power Sources* **2014**, *266*, 114–120.
- [98] H. Song, T.-G. Jeong, Y. H. Moon, H.-H. Chun, K. Y. Chung, H. S. Kim, B. W. Cho, Y.-T. Kim, *Sci. Rep.* **2014**, *4*, 4350.
- [99] S. Dong, X. Wang, L. Shen, H. Li, J. Wang, P. Nie, J. Wang, X. Zhang, *J. Electroanal. Chem.* **2015**, *757*, 1–7.
- [100] R. K. B. Gover, J. R. Tölichard, H. Tukamoto, T. Murai, J. T. S. Irvine, *J. Electrochim. Soc.* **1999**, *146*, 4348–4353.
- [101] I. Tsuyumoto, T. Moriguchi, *Mater. Res. Bull.* **2015**, *70*, 748–752.
- [102] W. Zhu, H. Yang, W. Zhang, H. Huang, X. Tao, Y. Xia, Y. Gan, X. Guo, *RSC Adv.* **2015**, *5*, 74774–74782.
- [103] Y.-Q. Wang, L. Gu, Y.-G. Guo, H. Li, X.-Q. He, S. Tsukimoto, Y. Ikuhara, L.-J. Wan, *J. Am. Chem. Soc.* **2012**, *134*, 7874–7879.
- [104] G. Vitiş, G. Kızıne, A. Lüsüz, J. Tiliks, *J. Solid State Electrochem.* **2002**, *6*, 311–319.
- [105] M. Vijayakumar, S. Kerisit, Z. Yang, G. L. Graff, J. Liu, J. A. Sears, S. D. Burton, K. M. Rosso, J. Hu, *J. Phys. Chem. C* **2009**, *113*, 20108–20116.
- [106] T. Zhang, B. Fuchs, M. Secchiaroli, M. Wohlfahrt-Mehrens, S. Dsoke, *Electrochim. Acta* **2016**, *218*, 163–173.
- [107] H.-G. Jung, S.-T. Myung, C. S. Yoon, S.-B. Son, K. H. Oh, K. Amine, B. Scrosati, Y.-K. Sun, *Energ Environ Sci* **2011**, *4*, 1345–1351.
- [108] J. Kim, S.-W. Kim, H. Gwon, W.-S. Yoon, K. Kang, *Electrochim. Acta* **2009**, *54*, 5914–5918.
- [109] C. C. Li, Q. H. Li, L. B. Chen, T. H. Wang, *ACS Appl. Mater. Interfaces* **2012**, *4*, 1233–1238.
- [110] D. H. Long, M.-G. Jeong, Y.-S. Lee, W. Choi, J. K. Lee, I.-H. Oh, H.-G. Jung, *ACS Appl. Mater. Interfaces* **2015**, *7*, 10250–10257.
- [111] L. Shen, H. Li, E. Uchaker, X. Zhang, G. Cao, *Nano Lett.* **2012**, *12*, 5673–5678.
- [112] L. Shen, C. Yuan, H. Luo, X. Zhang, S. Yang, X. Lu, *Nanoscale* **2011**, *3*, 572–574.
- [113] L. Yu, H. B. Wu, X. W. Lou, *Adv. Mater.* **2013**, *25*, 2296–2300.
- [114] S. Dsoke, B. Fuchs, E. Gucciardi, M. Wohlfahrt-Mehrens, *J. Power Sources* **2015**, *282*, 385–393.
- [115] S. Fleischmann, M. Zeiger, N. Jäckel, B. Krüner, V. Lemkova, M. Widmaier, V. Presser, *J. Mater. Chem. A* **2017**, *5*, 13039–1351.
- [116] J. Lee, A. Tolosa, B. Krüner, N. Jäckel, S. Fleischmann, M. Zeiger, D. Kim, V. Presser, *Sustainable Energy & Fuels* **2017**, *1*, 299–307.
- [117] A. Tolosa, B. Krüner, S. Fleischmann, N. Jäckel, M. Zeiger, M. Aslan, I. Grobelsek, V. Presser, *J. Mater. Chem. A* **2016**, *4*, 16003–16016.
- [118] F. X. Wang, S. Y. Xiao, Y. S. Zhu, Z. Chang, C. L. Hu, Y. P. Wu, R. Holze, *J. Power Sources* **2014**, *246*, 19–23.

Manuscript received: December 25, 2017
Accepted article published: January 30, 2018
Version of record online: February 26, 2018